Physical explanation for vibro-acoustic modulation in a structure due to local and global nonlinearities

Vom Promotionsausschuss der
Technischen Universität Hamburg
zur Erlangung des akademischen Grades
Doktor-Ingenieur (Dr.-Ing.)

genehmigte Dissertation

von
Lennart Dorendorf

aus
Hamburg

2023

Gutachter:
Prof. Dr.-Ing. habil. Marcus Rutner
Prof. Dr. rer. nat. habil. Norbert Hoffmann

Tag der mündlichen Prüfung: 25. August 2023

DOI: https://doi.org/10.15480/882.8717

ORCID: Lennart Dorendorf
https://orcid.org/0000-0003-0830-7982

HAMBURG UNIVERSITY OF TECHNOLOGY

Abstract

Physical explanation for vibro-acoustic modulation in a structure due to local and global nonlinearities

by Lennart Dorendorf

This dissertation suggests a physical explanation revealing why any elastic nonlinearity may cause vibro-acoustic modulation (VAM) in a dynamic system that is excited by two waves simultaneously (X_ω and X_Ω) in case the corresponding frequencies differ significantly ($\omega >> \Omega$): The low frequency (LF) vibration X_Ω activates the nonlinearity and varies quasi-statically the system's natural frequency ω_0 corresponding to the dominant mode shape. The amplitude and phase of the ultrasonic system response depend on the natural frequency ω_0 and are therefore modulated with low frequency Ω. This analytical explanation is built upon the assumption that the system reaches a steady-state vibration (constant amplitude and phase over time) due to ultrasonic excitation X_ω before the LF vibration X_Ω can change the dynamic properties of the system significantly. The fulfillment of this assumption is validated experimentally and numerically for an aluminum plate-like structure and excitation frequencies $\Omega = 10Hz \cdot 2\pi$ and $180kHz \cdot 2\pi < \omega < 230kHz \cdot 2\pi$: It is shown that the minimum and maximum amplitudes in the modulated ultrasonic system response match the respective steady-state amplitudes under static loading with a negligible error that is <1%. The beauty of the explanation is that it does not only work for the local nonlinear-elastic behavior of a defect, but also for any non-damage-induced (local or global) nonlinearity in the system which may cause modulation as well. The explanation is employed to conclude and demonstrate the following five analytical findings: 1) Any elastic nonlinearity may cause amplitude modulation and phase modulation at the same time. 2) The nonlinearity can cause envelope functions in the modulated system response with a variety of different characteristic shapes. 3) The maximum amplitude in the modulated system response in time domain can either coincide with the minimum or the maximum stress state corresponding to the LF vibration X_Ω. 4) Different nonlinearities in the same system can cause contrary modulations that neutralize

each other. 5) The steady-state evaluation of the ultrasonic system response allows—theoretically—VAM applications without exciting the LF vibration X_Ω. Finally, three nonlinearities in the same system are investigated separately: Two non-damage-induced nonlinearities (the variation of geometric stiffness and the nonlinear-elastic material behavior of aluminum) and one damage-induced nonlinearity (the contact of fatigue crack surfaces) are considered. Numerical simulations are carried out to quantify and compare the modulation they cause individually in the system response. The results comply with the analytical findings concluded from the physical explanation and emphasize that the conventional VAM evaluation for damage monitoring is error prone.

Contents

List of acronyms

AM amplitude modulation.

CFRP carbon fiber reinforced plastics.

FE finite element.

FFT fast Fourier transform.

LF low frequency.

MDOF multi-degree-of-freedom.

MI Modulation Index.

PM phase modulation.

SDOF single-degree-of-freedom.

SHM structural health monitoring.

VAM vibro-acoustic modulation.

List of symbols

ω	ultrasonic frequency (angular)	rad/s
Ω	low frequency (angular)	rad/s
X_ω	ultrasonic wave	
X_Ω	low frequency wave	
T_Ω	period corresponding to the low frequency wave	s
A_ω	amplitude of the ultrasonic wave	
A_Ω	amplitude of the low frequency wave	
$A_{\Omega,exp}$	amplitude of the low frequency wave (experimental)	
$A_{\Omega,num}$	amplitude of the low frequency wave (numerical)	
$A_{\omega\pm\Omega}$	sideband amplitude (in system response)	
D	dynamic magnification factor	$-$
θ	phase	rad
m	mass	kg
k	stiffness	N/m
F	force	N
ω_0	natural frequency (undamped system)	rad/s
ω_D	natural frequency (damped system)	rad/s
$\omega_{D,exp}$	natural frequency (damped system, experimental)	rad/s
$\omega_{D,num}$	natural frequency (damped system, numerical)	rad/s
β	frequency ratio ω/ω_0	$-$
d	damping coefficient	Ns/m
ξ	damping ratio	$-$
E	Young's modulus	N/m^2

I	second moment of inertia	m^4
ν	Poisson's ratio	$-$
ρ	material density	kg/m^3
α_R	mass-dependent Rayleigh damping coefficient	$-$
β_R	stiffness-dependent Rayleigh damping coefficient	$-$
r	fatigue stress ratio	$-$
A_{stat}	amplitude in system response (static loading)	
A_{dyn}	amplitude in system response (dynamic loading X_Ω)	
σ_X	stress in X-direction	N/m^2
ϵ_X	strain in X-direction	$-$
u_X	displacement in X-direction	m

Chapter 1

Introduction

The limitation of natural resources on planet earth is forcing mankind to become sustainable. At the same time engineers are expected to design infrastructure that guarantees safety. The conflict of these two demands poses a challenge. One approach to encounter this challenge is the employment of structural health monitoring (SHM) [7]: Reliable monitoring that allows accurate evaluation of structural integrity during service. The goal of SHM applications is to detect initiating damage early and to predict the remaining lifetime reliably. Successful monitoring improves safety and enables the extension of structural lifetime in service. Such lifetime extensions save resources in the long term.

Acoustic methods are successful in the SHM field, because they promise low-cost hardware implementation and applicability across different materials. Another advantage over competing methods is that their application does not have negative impacts on the environment. [7]

The acoustic methods that found their way into engineering industries utilize linear features of structural damage to detect it: They evaluate the reflection, scattering, transmission, attenuation and absorption of the excited wave [12, 16]. From an acoustics' perspective the term "linear method" indicates that the excitation frequency and the evaluated frequency are the same. The linear methods are facing one limitation in terms of sensitivity: The size of detectable damage is limited to the acoustic wavelength in the structure [7]. In order to overcome this limitation the scientific community tries to exploit the nonlinear behavior of structural damage for detection. In contrast to linear methods, the nonlinear acoustic methods evaluate frequencies that differ from the excitation frequencies. The vibro-acoustic modulation (VAM) method is a promising approach to do this: An ultrasonic wave X_ω with frequency ω and a low frequency (LF) vibration X_Ω with frequency Ω are introduced to the structure at the same time ($\omega >> \Omega$). The presence of nonlinear-elastic behavior (as exhibited by a variety of local defects) causes

the LF vibration X_Ω to modulate the ultrasonic wave X_ω in the structure. Such modulation manifests itself in frequency domain by the appearance of sidebands at $\omega \pm n \cdot \Omega$ where $n \in \mathbb{N}$. The VAM method utilizes the modulation of the ultrasonic wave to evaluate structural integrity. It was demonstrated in a large body of literature over the last three decades that the quantified modulation in the system response correlates with the initiation and growth of structural damage under favourable conditions—highlighting the method's potential [15, 16, 24, 70]. A superior sensitivity compared to linear acoustic methods was reported [21, 29, 34, 39, 46, 50, 53, 61, 71].

However, VAM has not yet found its way to SHM applications in the real world due to insufficient reliability and robustness. As reported in [20, 21, 39, 66], changing the boundary conditions and geometry, varying the excitation frequencies or altering sensor positions in laboratory setups can directly affect the success of damage detection with VAM. The major problem is that there are other non-damage-induced nonlinearities in any real SHM application that may cause modulation as well. Their nonlinear contribution to the system response potentially camouflages the output of local damage that one is actually interested in.

There is yet no comprehensive physical understanding revealing why and under what circumstances an elastic nonlinearity causes modulation in the system response [8, 53]. This lack of a physical explanation is motivating this thesis. Once the physical dependencies between the system and the modulation are understood the scientific community might be able to realize the method's potential or come up with even better ideas on how to utilize nonlinear behavior.

This dissertation is structured as follows: In section 2.1 the basics of the VAM method are introduced. Subsequently, the literature review in section 2.2 summarizes the scientific work on VAM. In chapter 3 the physical explanation is presented showing why elastic nonlinearities cause modulation. This is the cornerstone of the dissertation. First, the explanation is given for a damped nonlinear single-degree-of-freedom (SDOF) system in section 3.1. Second, it is explained in section 3.2 how this explanation is applicable to a multi-degree-of-freedom (MDOF) system. The explanation is based on one major assumption. In chapter 4 this assumption is proven to be true experimentally and numerically for an aluminum plate-like structure. Further, the limits of the explanation's applicability are discussed. There are at least five analytical findings that can be derived directly from the suggested physical explanation. These findings are presented, demonstrated and discussed in

chapter 5. In chapter 6 three different nonlinearities in the same aluminum structure are investigated separately: The variation of geometric stiffness, the nonlinear-elastic material behavior of aluminum and the contact of local fatigue crack surfaces. On the one hand, the goal in chapter 6 is to explain and demonstrate why nonlinear-elastic behavior is exhibited under tensile fatigue loading. On the other hand, the author aims to quantify and compare the modulation caused by these individual nonlinearities in the same aluminum specimen. The results comply with the analytical findings and emphasize that the conventional VAM evaluation for damage monitoring is error prone. The thesis is summarized in chapter 7.

Chapter 2

Vibro-acoustic modulation

This chapter introduces the VAM method. In section 2.1 the basic idea of the monitoring approach is described and demonstrated with experimental results from an aluminum structure under fatigue loading. Section 2.2 overviews the scientific literature on VAM and summarizes the state of research.

2.1 Evaluating structural integrity with VAM

The VAM method is shown schematically in figure 2.1. Two waves are introduced to the same structure simultaneously. On the one hand, an ultrasonic wave X_ω with frequency ω and amplitude A_ω is excited. On the other hand, a low frequency (LF) wave X_Ω with frequency Ω and amplitude A_Ω is excited. The waves differ significantly in terms of their frequency ($\omega >> \Omega$) and in terms of their amplitude ($A_\omega << A_\Omega$). In a structure of perfectly linear behavior a pure superposition of X_ω and X_Ω would occur. In frequency domain the superposed system response would then only contain the frequency components ω and Ω (figure 2.1, bottom-left). If, however, the structure behaves nonlinearly, the ultrasonic wave X_ω is modulated by the LF vibration X_Ω. In frequency domain this modulation manifests itself by the occurrence of sidebands at the frequencies $\omega \pm n \cdot \Omega$ where $n \in \mathbb{N}$ (figure 2.1, bottom-right). It has been shown that the local characteristics of material defects in a structure—like local cracks whose contact surfaces vary with the opening and closing of the crack—can cause nonlinear effects in the global system response [12] such as modulation of the ultrasonic wave X_ω.

In order to quantifiy the modulation in the system response the ratio of sideband amplitudes $A_{\omega\pm\Omega}$ and the amplitude A_ω is used. Arguably, the most popular parameter quantifying modulation is the Modulation Index (MI), defined by Donskoy in [12] and given in equation 2.1.

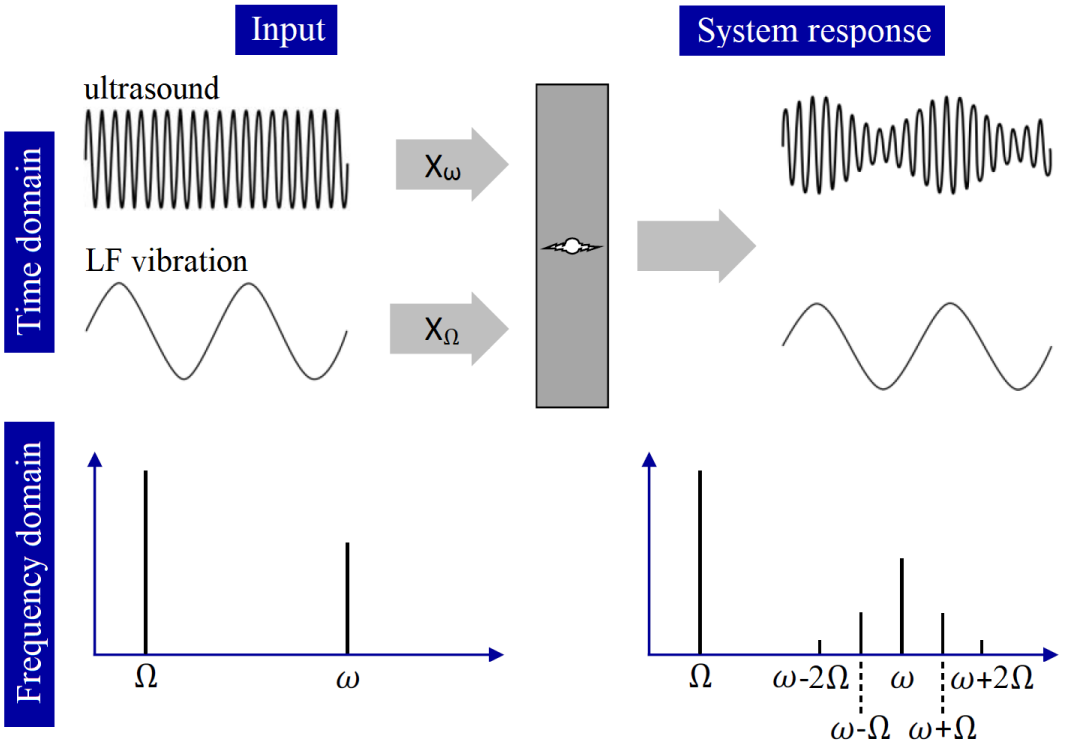

FIGURE 2.1: Vibro-acoustic modulation method schematically: A structure is excited with an ultrasonic wave X_ω and a low frequency vibration X_Ω simultaneously. The modulation of the ultrasonic system response manifests itself by the appearance of sidebands in the corresponding FFT spectrum at frequencies $\omega \pm n \cdot \Omega$ where $n \in \mathbb{N}$.

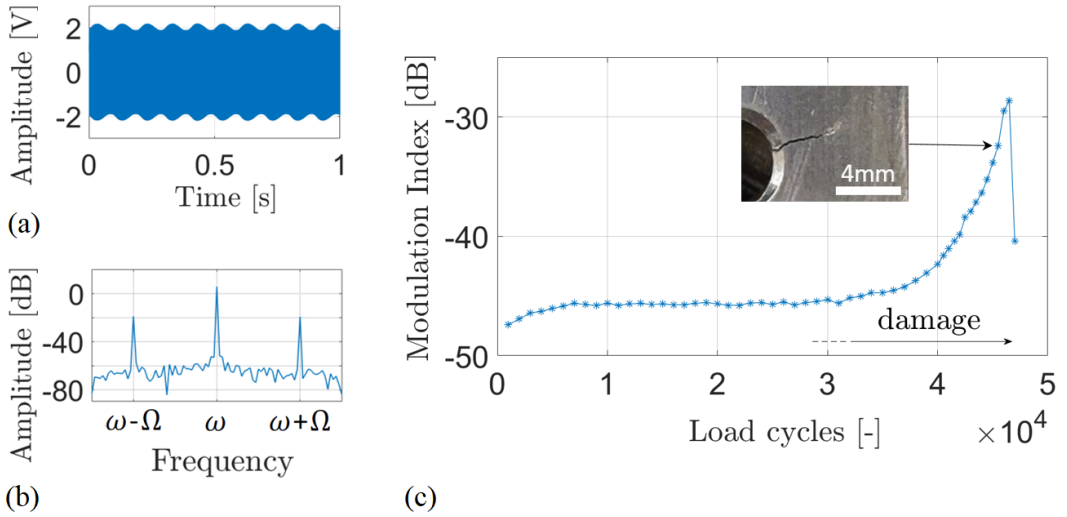

FIGURE 2.2: (a) Experimental system response in time domain over 1s measured with an aluminum specimen shortly before fatigue failure (b) Corresponding FFT spectrum (c) Modulation Index over fatigue load cycles, fatigue failure after 47000 load cycles

$$MI = 20 \cdot log_{10}\left(\frac{A_{\omega-\Omega} + A_{\omega+\Omega}}{2A_{\omega}}\right) \tag{2.1}$$

Figure 2.2a shows a (highpass-filtered) system response that was measured experimentally over one second with an aluminum specimen shortly before fatigue failure. The corresponding fast Fourier transform (FFT) spectrum is plotted in figure 2.2b. When evaluating the MI over the fatigue load cycles (representing its lifetime), one can observe an experimental result as shown in figure 2.2c under favourable conditions. The exponential increase of the MI before the damage becomes visible to the bare eye promises sensitive SHM applications.

Note that for any real VAM application modulation will be measured already in a pristine state (cycle 0 in figure 2.2c). This initial modulation is caused by known and/or unknown non-damage-induced nonlinearities in the dynamic system. In order to detect local damage later during the lifetime of a structure (here: fatigue crack in aluminum) the modulation caused by the damage needs to increase the initially measured modulation significantly.

2.2 Literature review

The idea to evaluate VAM for damage detection evolved in the 1990s: Rudenko and Chin [55] described in 1994 the nonlinear-elastic behavior of two rough surfaces in contact. On this basis Zaitsev et al. [70] proposed in 1995 to utilize such nonlinear behavior to detect cracks in metal. They suggested to apply an ultrasonic wave (X_{ω}) and a LF vibration (X_{Ω}) simultaneously to analyze nonlinear manifestations in the system response. Nazarov and Sutin [47] calculated the nonlinear-elastic (mechanical) properties of a solid with cracks in 1997.

In 1998 Donskoy and Sutin [15] published first experimental results on the VAM method: They reported the successful distinguishment of an integer weld in a steel pipe joint from a defective one. A $20kHz$ ultrasonic wave (X_{ω}) and a $30Hz$ vibration (X_{Ω}) were introduced to the joint. The spectrum of the system response corresponding to the defective weld showed two significant pairs of sidebands while the spectrum corresponding to the integer weld showed none. It was demonstrated experimentally for the defective weld that the amplitudes of the sidebands $A_{\omega\pm\Omega}$ correlate linearly with the excitation amplitude A_{ω}. It was already stated in this early publication that the detection method is—in principle—applicable to any contact-type defect

that exhibits nonlinear behavior such as cracks, debondings and delaminations.

Donskoy et al. [17] applied the VAM method in the same year (1998) to detect cracks and corrosive degradation in (steel) reinforced concrete. There have been numerous publications since then until today demonstrating the potential of VAM to identify damage in concrete or mortar [10, 31, 45, 64, 65].

In 2000 Zaitsev and Sas [69] reported that the modulation in an aluminum plate with a single crack (crack length $5mm$) is significantly higher compared to the modulation in the (identical) pristine plate. It was stated that the observed modulation strongly depends on the ultrasonic excitation frequency ω. Spectra with up to 15 pairs of sidebands were shown for the defective plate. In some cases, the sidebands' amplitudes rose above the amplitude of the ultrasonic excitation frequency ($A_{\omega\pm\Omega} > A_{\omega}$). The relationship of the LF amplitude A_{Ω} and the modulation in the ultrasonic system response was investigated as well. The results showed a linear dependency. Interestingly, this paper plotted the temporal record of the modulated ultrasonic system response vs. the LF vibration in time domain. It revealed that the maximum amplitude of the modulated system response coincided with the lowest stress level of X_{Ω} in this case.

In the same year (2000) Van den Abeele et al. [61] presented experimental investigations on crack detection in plexiglas and sandstone samples with VAM. The observed modulation in the cracked samples was significantly higher than in the uncracked samples. It was stated in this publication that the exhibited (non-damage-induced) "atomic" nonlinearity of pristine aluminum, steel and plexiglas is very weak and that resultant modulation is therefore difficult to measure. Note that more recent publications disconfirmed the latter statement, as this literature review will unfold.

In 2001 Donskoy et al. [16] presented comprehensive experimental work on the VAM method: Herein, they reported successful detection of fatigue cracks in steel bars. They confirmed the previously published linear dependency of the spectral amplitudes $A_{\omega\pm\Omega}$ and A_{ω}. On this basis, they suggested to use the ratio $A_{\omega\pm\Omega}/A_{\omega}$ to quantify modulation—and hereby proposed the MI for the first time. It was demonstrated experimentally that the quantified modulation correlates with the size of the fatigue crack. It was this finding that emphasized the method's potential for SHM applications. Furthermore, the dependency of the modulation on the LF amplitude A_{Ω} was investigated. The linear dependency—previously reported by Zaistev et al. in [69]—was only confirmed for moderate amplitudes A_{Ω} in this

paper. Note that the LF vibration X_Ω was excited with an electromagnetic shaker that introduces bending mode shapes to the specimen. The first three bending mode shapes were investigated in [16]. It was concluded that the vibrational mode shape corresponding to the LF excitation X_Ω has to affect the stress state of the fatigue crack to modulate the ultrasonic system response[1].

In the following two decades the optimistic tone throughout VAM-related publications weakened a little. The upcoming scientific publications clarified that the reliability of the method for real-world applications is at least questionable [20, 21, 39, 54, 66, 68]:

In 2006 Duffour et al. [20] presented an experimental study towards the sensitivity and reliability of the VAM method regarding the detection of fatigue cracks in steel beams. The method was applied to cracked and pristine samples for direct comparison. The LF vibration X_Ω was introduced by an electromagnetic shaker exciting the first (bending) mode shape. In contrast to previous publications the authors did not present eye-catching VAM spectra for one specific excitation frequency ω, but evaluated the method over a wide range of ultrasonic frequencies $50kHz < \omega/(2\pi) < 200kHz$. The ratio $A_{\omega\pm\Omega}/A_\omega$ (quantified modulation) was measured for each excitation frequency ω (at intervals of $\Delta\omega = 0.2kHz \cdot 2\pi$) and plotted over the frequency range $180kHz < \omega/(2\pi) < 200kHz$. Comparison of this curve for a cracked sample with the respective curve for a pristine sample was discouraging: A vertical offset (difference in modulation) was not visible. There were many excitation frequencies ω for which the quantified modulation in the cracked sample was significantly higher. However, there were many frequencies ω as well for which the quantified modulation in the cracked sample was significantly lower. The authors concluded that—even when considering the average modulation over the range of frequencies ω—a distinguishment of the samples (detection of the crack) seemed impossible for the investigated setup. The authors assumed that nonlinearities exhibited by the contact of the specimen with supports and contact with the shaker caused modulation that prevented successful damage detection. In order to eliminate these non-damage-induced nonlinearities they developed a second setup in which the specimen was hanging from elastic strings. The LF vibration X_Ω was not excited continuously by the shaker, but introduced by a single impact of a

[1] The experimental and numerical work in this dissertation does not excite bending waves by introducing X_Ω. In fact, X_Ω is applied as longitudinal stress in the scope of this dissertation. By doing so, the author keeps things simple, because it assures that the fatigue cracks are always affected in the same manner—by stress acting perpendicularly to the crack surfaces. Therefore, the amplitude of the stress variation at the crack does not depend on the frequency Ω.

hammer[2]. For this second setup the authors reported a more successful crack detection but stated that the correlation of the crack size with modulation is fairly poor. They concluded that the experimental test setup is crucial for reliable damage detection with VAM.

Polimeno and Meo [54] investigated experimentally in 2008 how the boundary conditions of a specimen affect the modulation in pristine samples. The results showed that the contact between the holding clamps and the structure can generate modulation that causes false-positive indication of damage in a pristine sample. They concluded that future work is necessary to distinguish the modulation that is caused by non-damage-induced nonlinearities (such as the described contact) and damage-induced modulation.

In 2009 Zaitsev et al. [68] discussed factors limiting the sensitivity of the VAM method: The "atomic" (material) nonlinearity and the nonlinear behavior of the electronic equipment (including sensors and their coupling to the specimen) were expected to cause modulation jeopardizing successful crack detection.

Yoder et al. [66] suggested in 2010 to utilize a frequency-swept ultrasonic excitation X_ω for VAM to improve the robustness of the method for crack detection in steel beams. A similar approach was investigated by Dziedziech et al. [22].

Klepka et al. [37] wrote in 2012 that modulation may not only result from cracks but also from non-damage-induced nonlinearities including friction, overloads, the interface of sensors with the structure and the electronic instrumentation in the measurement chain. It was concluded that physical understanding of these nonlinearities is necessary to enable VAM engineering applications.

In 2016 Liu et al. [43] suggested to evaluate the spectral correlation function (instead of the spectrum) of the system response to establish baseline-free non-destructive testing with VAM. In their conclusion they stated that the proposed methodology only enables reliable damage detection in linear systems. Hence, any other nonlinearity in the system (despite occurring damage) jeopardizes the method's success. A similar baseline-free approach was investigated recently in [13].

Dunn et al. [21] addressed in 2017 critical aspects for damage detection with VAM. They concluded that VAM has great potential due to unmatched

[2]Note that such an impact primarily excites the first bending mode shape and therefore represents a comparable method here.

sensitivity, but that experimental parameters have to be selected and optimized with extreme care to ensure reliable damage detection.

In 2017 Lim et al. [39] formulated necessary conditions for successful crack detection with VAM in aluminum plates: They argued that—when assuming a steady-state vibration due to the ultrasonic excitation X_ω—the crack must be located in an anti-node of the bending vibration mode corresponding to ω to cause modulation. They used a laser vibrometer to demonstrate that the modulation in the system response is significantly higher when the crack is located in an anti-node than when located in a node of the bending mode. Investigations by Liu et al. [41] in 2020 support this finding. However, the results of Lim et al. in [39] also indicated that the fulfillment of the described necessary condition does not guarantee success. They concluded that the modulation of other nonlinearities—such as the material nonlinearity of aluminum—have to be suppressed by the choice of suitable excitation frequencies as well for reliable damage detection.

Dziedzich et al. [23] stated in 2021 that the separation of nonlinear effects into damage-related ones and non-damage related ones (including material nonlinearity and nonlinear boundary conditions) is a crucial task to enable real-world VAM applications.

At this point of the literature review it can be summarized that the insufficient reliability of the method appears to be the major issue limiting VAM applications. Non-damage-induced nonlinearities cause modulation that jeopardizes successful damage detection. It is the author's belief that this problem should be addressed by explaining why an elastic nonlinearity causes modulation in the dynamic system of interest. Once this is understood the next step is to identify all nonlinearities that are present in the system. This includes damage-induced and non-damage-induced nonlinearities. For each of them one should be able to estimate the amount of modulation they cause individually in that specific system. Only on this basis the potential of the VAM method for reliable damage monitoring can truly be discussed. The described lack of a physical understanding motivates this dissertation: The author suggests a simple analytical explanation that is applicable to any elastic nonlinearity in a dynamic system (chapter 3). Further, this dissertation aims to investigate and compare three different nonlinearities in the same system separately. This includes one damage-induced nonlinearity (contact of fatigue crack surfaces) and two non-damage-induced nonlinearities (the variation of geometric stiffness and the nonlinear-elastic material behavior of aluminum).

Despite the lack of a physical understanding and the insufficient reliability of the method there is a large body of literature on VAM targeting other research goals. The author attempts to summarize such scientific work—that was not mentioned previously—in the following.

In 2008 Meo et al. [44] employed the VAM method to detect barely visible impact damage in carbon fiber reinforced plastics (CFRP). Low velocity impacts cause delaminations (debonding) of single layers beneath the visible surface of the structure. Detection of impact damage in composites is a major challenge in the modern aerospace industry. The authors demonstrated for CFRP laminates that—when exciting suitable frequencies ω and Ω—the modulation in the system response is significantly higher than in pristine laminates. There have been numerous publications since then until today demonstrating the potential of VAM for damage detection in composites [3, 26, 33, 36, 48, 63].

In recent years there were ambitions in the scientific community to employ the VAM method not only to detect and monitor, but also to localize damage [9, 30, 52, 57].

Since 2018 the use of machine learning on VAM data was exploited to improve the method [6, 25, 38, 40, 42, 45].

It was already stated in earliest VAM publications [16, 70] that the nonlinear behavior of damage is expected to cause AM and PM in the system response. While most studies evaluated the sidebands in the spectrum, Hu et al. [27] investigated in 2010 the occurrence of AM and PM separately in time domain. They concluded on the basis of experimental results with aluminum plates that structural damage does cause AM and PM, but that AM correlates far better with the crack size. Despite this result there have been ambitions since then to utilize PM instead of AM for damage detection [14, 18, 35, 42]. The motivation for these ongoing investigations seems to be the hypothesis that fatigue cracks cause primarily PM in their initial state [42]. Contrarily, Oppermann et al. (including the author of this dissertation) [49] argued in 2021 that the dominant modulation type in the system response (AM or PM) cannot be an indicator for the type of nonlinearity (e.g. a crack). They demonstrated this theoretically by showing that the dominant modulation type caused by a crack can either be AM or PM—depending on the geometry (e.g. sensor location) of the system.

Despite thirty years of research there are—to the author's best knowledge—no real-world VAM applications reported in the literature. However, there were practical ideas: In 2014 Kim et al. [33] suggested to employ operational

loads in structures as LF excitation X_Ω. Wind turbine blades were considered for such an application: In order to monitor their integrity during service one could utilize the bending stress variation in the blade due to the operational rotation. Hence, only the excitation of the ultrasonic wave X_ω would be necessary. They validated the practicability of their idea on a laboratory setup: A small-scale turbine with three CFRP blades (rotor diameter $2.1m$) was installed in front of a wind tunnel. In this setup the "operational" vibration frequency was $\Omega = 3Hz \cdot 2\pi$. The VAM spectra of a cracked turbine blade and a pristine one were compared. The authors stated that—when exciting a favourable ultrasonic excitation frequency ω—a stronger modulation was observed for the damaged blade. Alnutayfat et al. [1] complemented this idea in 2023: They argued that the interaction of the wind turbine blade surface and environmental air turbulence causes ultrasonic vibrations during service that could be employed as X_ω. At the same time the variation of the bending stress due to the operational rotation could be utilized as LF vibration X_Ω, as suggested previously. Consequently, it was argued that no waves need to be excited actively in the structure to apply VAM. The challenge in this scenario is to measure the (altering) operational vibrations in the structure with sensors and use such data for VAM evaluation. In order to validate the general feasibility of this approach, the authors presented experimental results on laboratory steel samples with dimensions $254mm/25.4mm/3.175mm$ that were excited actively.

In the author's opinion the latter experimental setup emphasizes how far this idea is yet from real-world applications. Additionally, note that utilizing operational loads and vibrations for VAM applications as suggested in [33] and [1] comes with a cost: One loses the freedom to choose suitable frequencies for evaluation. The previous literature review emphasized that the frequency selection—especially regarding the ultrasonic one—strongly affects the method's success.

The frequencies in the scientific literature employed for VAM vary significantly: "Low" frequencies in experimental setups corresponding to X_Ω are reported in the range $3Hz < \Omega/(2\pi) < 60kHz$ [33, 39]. They are applied with tensile hydraulic machines [12], electromagnetic shakers [36] or piezoceramics [39]. Values of the "high" excitation frequency corresponding to X_ω vary in the range $20kHz < \omega/(2\pi) < 4.8MHz$ [15, 60].

Dziedzich et al. [23] presented in 2021 a successful study on a thermal analogy of the VAM method: A periodic thermal field was applied to aluminum plates with fatigue cracks, representing the LF excitation X_Ω. This

varying thermal field was excited by a modulated laser source. The ultrasonic excitation X_ω was excited with a piezo as is common practice in the VAM literature. The system response was measured with a laser vibrometer.

Alnutayfat et al. [2] proposed in 2022 a different indicator for damage monitoring with VAM. They suggested to evaluate the number n of occuring sidebands with $\omega \pm n \cdot \Omega$ where $n \in \mathbb{N}$ in the spectrum instead of the conventional MI. They reported that—for some of the tested steel samples—the number n showed better damage indication than the MI.

Finally, the author of this dissertation wants to point out that it is an ongoing research goal to understand the exact mechanisms that lead to the nonlinear-elastic behavior of contact-type defects [8, 37]. The discussed and investigated mechanisms include Hertzian contact at (microcrack) surface asperities [4, 9, 12, 23, 32, 55, 58], so called "clapping" or "breathing" (opening-closing of a crack) [9, 23, 29, 32, 35, 36, 37, 53] and energy-dissipative mechanisms [9, 12, 23, 36, 37, 53, 62, 67, 69] such as hysteresis. Note that an ultimate understanding of the mechanisms leading to nonlinear-elastic behavior of a specific crack is not necessary to employ VAM for its detection. As long as one is certain that the crack does behave in a nonlinear-elastic manner (for whatever reasons) one can employ the method. The physical explanation in chapter 3 of this dissertation does not aim to explain the mechanisms leading to nonlinear-elastic behavior. In fact, it aims to explain why any elastic nonlinearity (local or global) causes modulation in a specific dynamic system.

Chapter 3

Physical explanation

The physical explanation is presented for a damped nonlinear SDOF system in section 3.1. Afterwards, it is explained in section 3.2 how this explanation is applicable to a MDOF system. Note that the content presented in this chapter was partially published by Dorendorf et al. in 2022 [19].

3.1 Single-degree-of-freedom system

A damped SDOF system with mass m, stiffness $k(x)$ and damping coefficient d is considered (figure 3.1a). The system is nonlinear, because its stiffness k depends on the displacement x (figure 3.1b).

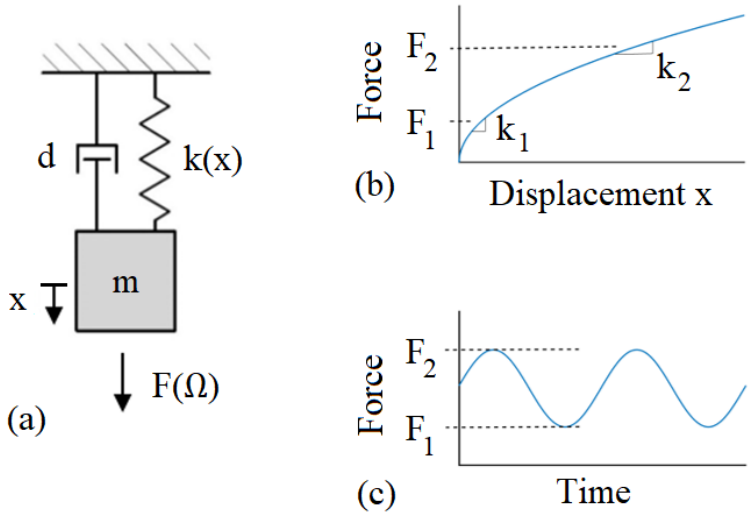

FIGURE 3.1: (a) Damped SDOF system: mass m, damping coefficient d, stiffness $k(x)$, displacement x, force $F(\Omega)$ (b) Nonlinear-elastic relationship between force F and displacement x (c) Force F over time representing the LF excitation X_Ω

The LF excitation X_Ω is represented by the force $F(\Omega)$ here. It is a tensile force that varies harmonically and slowly (quasi-statically) between the values F_1 and F_2 over time (figure 3.1c). Consequently, also the stiffness k

varies between the values k_1 and k_2 over time with frequency Ω. For a fixed stiffness k, the natural frequency ω_D of the damped (linear) SDOF system is known (equation 3.1). Herein, ω_0 is the natural frequency of the corresponding undamped system given in equation 3.2. The damping ratio ξ is defined in equation 3.3.

$$\omega_D = \omega_0 \sqrt{1 - \xi^2} \tag{3.1}$$

$$\omega_0 = \sqrt{\frac{k}{m}} \tag{3.2}$$

$$\xi = \frac{d}{2m\omega_0} \tag{3.3}$$

Since $k(x)$ is varied over time with frequency Ω, also the natural frequencies ω_D and ω_0 vary over time with frequency Ω. The explanation suggested in the following is based on one major assumption: Since $\omega >> \Omega$, the global system response caused by the excitation with the ultrasonic wave X_ω reaches a steady-state response before the LF excitation $F(\Omega)$ can change the stiffness $k(x)$ of the system significantly. Therefore, one can evaluate the steady-state response (caused by the ultrasonic excitation X_ω) regarding amplitude and phase for a linear system with fixed stiffness k ($A_\omega << A_\Omega$), while only producing a negligible error. It is proven experimentally and numerically in chapter 4 that the major assumption is valid for the aluminum specimens investigated in the scope of this dissertation.

For the damped SDOF system with linear properties, the analytical solutions for the dynamic magnification factor D (proportional to the amplitude) and the phase θ of the steady-state response are known [11] and given in equations 3.4 and 3.5. Both depend on β, defined as the ratio of excitation frequency ω and the natural frequency of the undamped system ω_0 (equation 3.6).

$$D = \frac{1}{\sqrt{(1 - \beta^2)^2 + (2\xi\beta)^2}} \tag{3.4}$$

$$\theta = arctan \frac{2\xi\beta}{1 - \beta^2} \tag{3.5}$$

$$\beta = \frac{\omega}{\omega_0} \tag{3.6}$$

The magnification factor D, which is proportional to the amplitude of the steady-state response, is plotted over the frequency ratio β and the damping ratio ξ in figure 3.2a. The phase θ of the steady-state response is plotted over β and ξ in figure 3.2b. Note that even small changes in the ratio β will have a significant effect on the amplitude (represented by D) and the phase θ.

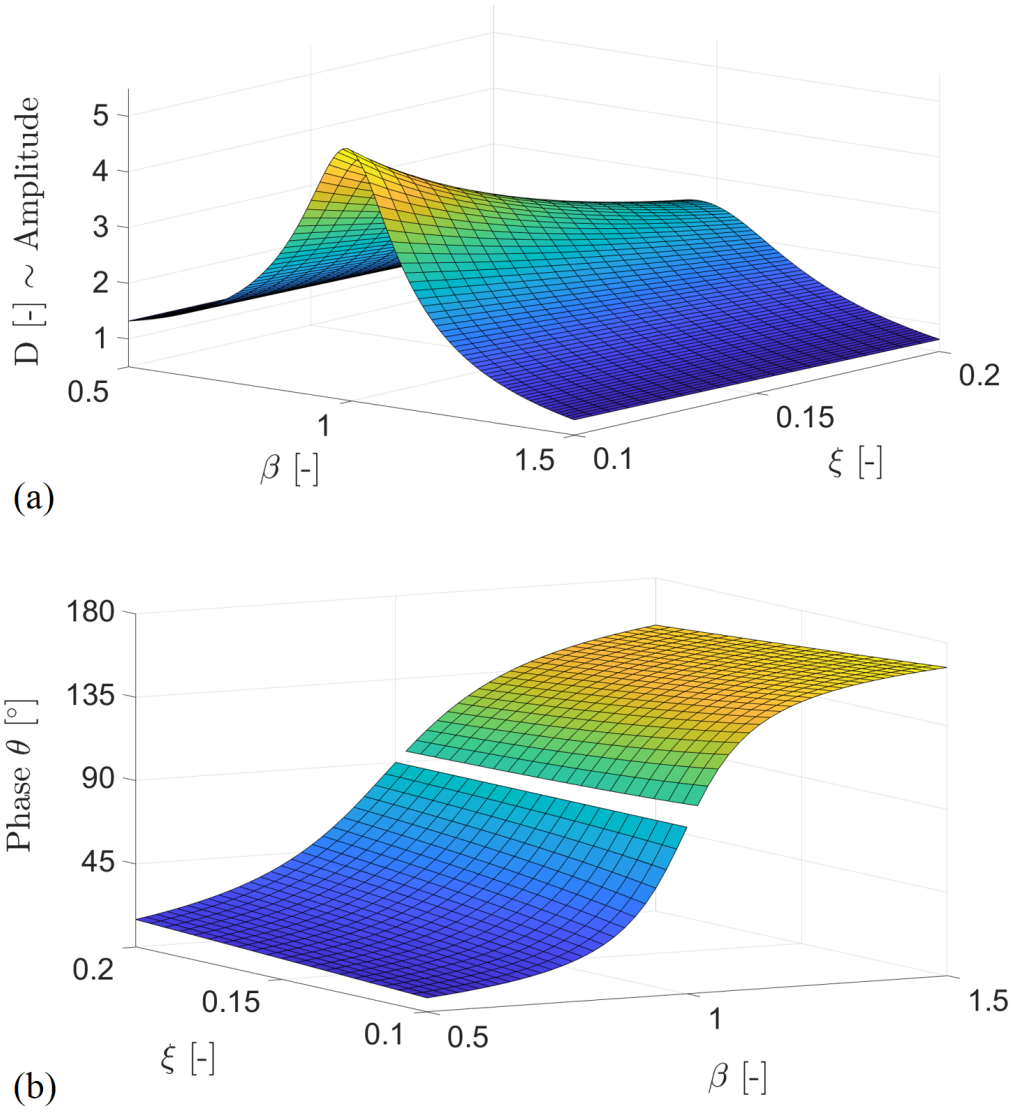

FIGURE 3.2: (a) Dynamic magnification factor D (proportional to the amplitude of the steady-state response) over ratio $\beta = \omega/\omega_0$ and damping ratio ξ (b) Phase θ of the steady-state response over ratio $\beta = \omega/\omega_0$ and damping ratio ξ [19]

As stated above, the slow (quasi-static) change in stiffness $k(x)$, caused by the LF excitation $F(\Omega)$, will vary $\omega_0(\Omega)$ over time with frequency Ω. Since the excitation frequency ω is constant when employing the VAM method, this leads to a variation of the ratio $\beta(\Omega)$ over time with frequency Ω between

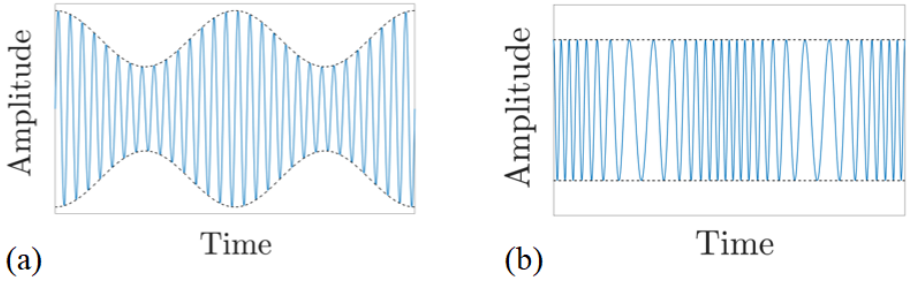

FIGURE 3.3: (a) Amplitude modulation schematically (b) Phase modulation schematically [19]

the values β_{min} and β_{max}. And thus, taking into account figure 3.2a and figure 3.2b, will cause AM and PM over time, as shown schematically in figure 3.3a and figure 3.3b. The analytical computations for the generation of AM and PM in a nonlinear SDOF system can be found in appendix A.

Both types of modulation (AM and PM) will potentially cause an infinite number of sidebands in the FFT spectrum at frequencies $\omega \pm n \cdot \Omega$ where $n \in \mathbb{N}$.

3.2 Multi-degree-of-freedom system

When considering a real structure, there is an infinite number of degrees of freedom and therefore an infinite number of natural frequencies with corresponding mode shapes. The global system response will be dominated by the natural frequencies and mode shapes that lie closest to the excitation frequency ω. The suggested physical explanation is applicable to each single natural frequency contributing to the system response. The system response will be determined by the superposition of those single contributions. For each modal contribution the system response can be determined using the above-discussed SDOF system. The mass, stiffness and load in the SDOF system correspond to the respective modal properties. Note that the loading position in the MDOF system will affect the amplitude of the modal load in the SDOF system. In case the loading position is located in a node of the corresponding mode shape, the modal load will be zero. In case the loading position is located in an anti-node (peak) of the corresponding mode shape, the magnitude of the modal load will be at maximum.

Due to the superposition of modal contributions, the physical explanation is applicable to a MDOF system. The experimental and numerical investigations in the following chapters 4 and 5 demonstrate this.

In the author's opinion, it makes sense to differentiate two cases of nonlinear MDOF systems here: 1) The system exhibits nonlinear-elastic behavior globally. This would apply for example when considering a structure made of a material with nonlinear-elastic stress-strain behavior. According to the suggested explanation, strong modulation is expected for this structure (already in a pristine state). This is an example for modulation caused by a non-damage-induced nonlinearity, as demonstrated and discussed in section 6.3. 2) Only a local part of the structure exhibits nonlinear-elastic behavior. This case applies to most SHM applications where the VAM method is employed to measure modulation in the global system response, caused by local defects exhibiting nonlinear-elastic behavior. Considering the suggested explanation, note that this local nonlinearity must be strong enough to vary the natural frequencies of the global structure when activated by the LF vibration X_Ω. Further, the defect position will affect how much the local nonlinearity can vary a natural frequency ω_0. In case the defect is located in a node of the corresponding mode shape, the effect will be at minimum. In case the defect is located in an anti-node (peak) of the corresponding mode shape, the effect on the variation of the natural frequency will be at maximum.

Chapter 4

Validation and limits

The explanation presented in chapter 3 is built upon one major assumption: The vibration due to the ultrasonic excitation X_ω reaches a steady-state (constant amplitude and constant phase over time) before the LF vibration X_Ω can change the dynamic properties of the system significantly. The goal of the investigations in this chapter is to validate this assumption experimentally and numerically for an aluminum specimen under tensile fatigue loading. The experimental and numerical setups are described in section 4.1. The investigations' results validating the assumption are presented in section 4.2. Afterwards, the results are taken into account to discuss the limits of the explanation's applicability in section 4.3.

4.1 Experimental and numerical setup

The experimental and numerical studies are carried out for flat aluminum specimens with a thickness of $t = 3mm$. The geometry is shown in figure 4.1a. Note that all experimental and numerical work carried out in the scope of this dissertation complies with this specific dynamic system and geometry.

For experimental testing two piezoceramics (PI ceramics, thickness $2mm$, diameter $10mm$, product PRYY+0372) are used [51]. One of them is employed to excite X_ω with ultrasonic frequency ω in the range $170kHz \cdot 2\pi < \omega < 230kHz \cdot 2\pi$. The other piezoceramic is used to measure the system response (s. figure 4.1b). The LF excitation X_Ω with $\Omega = 10Hz \cdot 2\pi$ is excited with a tensile hydraulic machine ($F_{min} = 0kN$; $F_{max} = 1.5kN$; fatigue stress ratio $r = 0$). Both ends of the specimen are clamped into the machine.

Numerical studies are carried out with FE software Abaqus CAE 2018 [56]. The defined material properties comply with the aluminum tested experimentally. The Young's modulus is $E = 7000kN/cm^2$, the Poisson's ratio is $\nu = 0.296$ and the density is $\rho = 2752kg/m^3$. The damping ratio is set

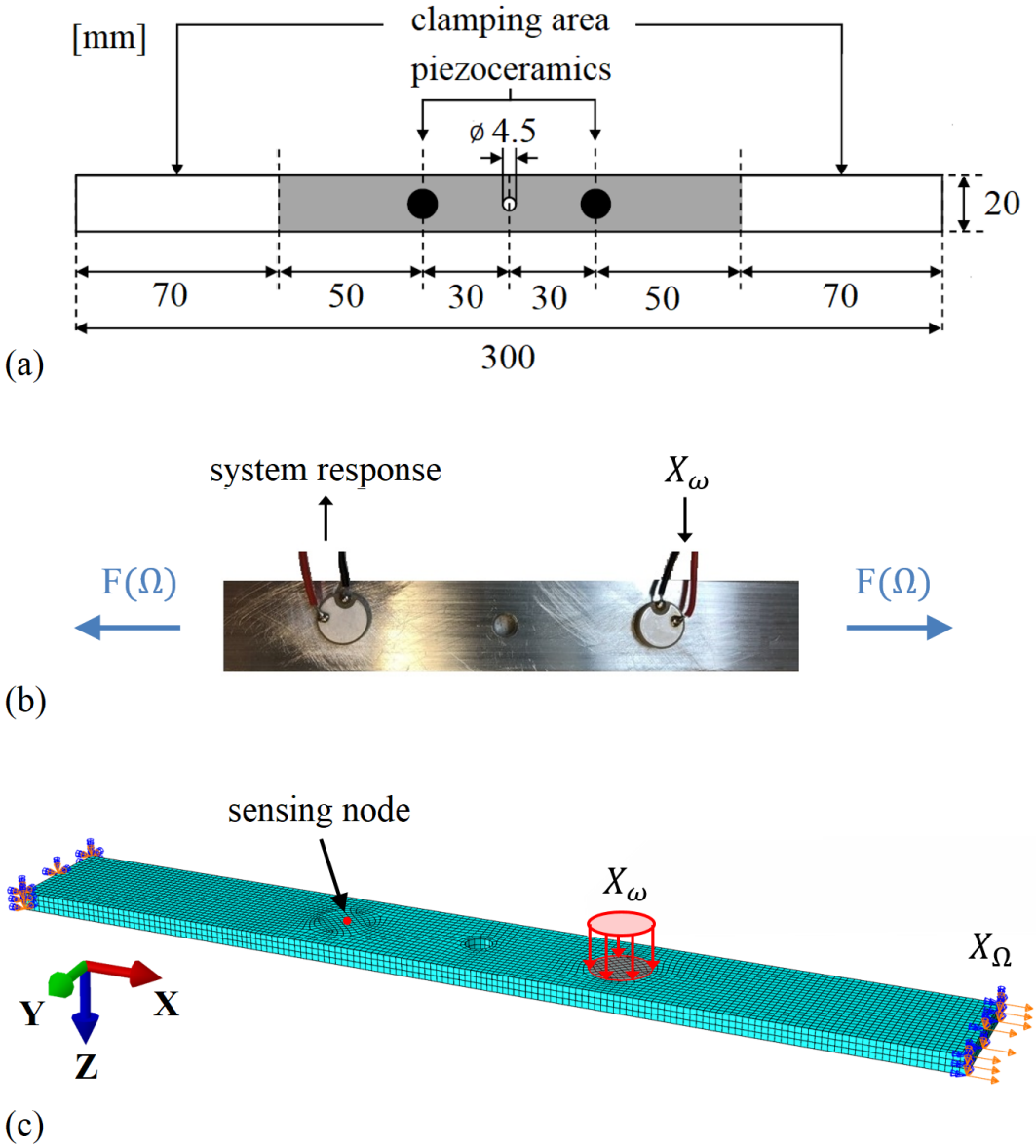

FIGURE 4.1: (a) Specimen geometry in mm (thickness $t = 3mm$) (b) Experimental aluminum specimen with piezoceramics (not the entire specimen is shown here) (c) FE model in Abaqus CAE with dimensions $160mm/20mm/3mm$

to $\xi = 0.01$ for the frequency range of interest with Rayleigh damping coefficients $\alpha_R = 80$ and $\beta_R = 1.38 \cdot 10^{-8}$. To apply the ultrasonic excitation X_ω in the FE model, a pressure is acting on the circular surface (diameter $10mm$) of the specimen, representing the piezoceramic position. This pressure acts orthogonal to the surface. As a system response, the out-of-plane acceleration in Z-direction $[m/s^2]$ at a specific node on the specimen's surface is evaluated. This node is highlighted in figure 4.1c and referred to as the "sensing node" from hereon. The LF vibration X_Ω is excited as a prescribed displacement in X-direction applied to the cross-section at the right

end of the structure in figure 4.1c.

Note that instead of evaluating the ultrasonic system response in multiple locations of the specimen, the excitation of multiple ultrasonic frequencies ω is analyzed and the system response is evaluated only at one location of the specimen. The latter leads to a similar variety of results and is common practice in the literature [7, 66].

4.2 Validation of the major assumption

First, the results of a modal analysis, carried out experimentally with a 3D scanning laser vibrometer (PSV 500-3D-M, Polytec), are compared to the results of a numerical modal analysis performed with Abaqus CAE. Figure 4.2a shows one mode shape found experimentally for the natural frequency $\omega_{D,exp} = 171kHz \cdot 2\pi$. The same mode shape was found numerically with Abaqus CAE for $\omega_{D,num} = 168kHz \cdot 2\pi$ (figure 4.2b). The fact that these frequencies only differ by 2% demonstrates the accuracy of the defined material properties in the FE model.

In a second step, the specimen is excited experimentally with the ultrasonic excitation X_ω where $\omega = 170kHz \cdot 2\pi$ (LF excitation X_Ω is not present). The measured system response (measured with a piezoceramic) is plotted over $3ms$ in figure 4.2c. It can be seen that a steady-state response (amplitude constant over time) is reached already within roughly $1ms$. The comparative numerical (explicit, dynamic) FE analysis shows a steady-state response even earlier (figure 4.2d). The numerical simulation is only run for $1ms$ to reduce computational costs. Note that $1ms$ is only $1/100$ of $T_\Omega = 1/10Hz = 0.1s$ ($\omega >> \Omega$).

In a third step, the validation of the major assumption from section 3.1 is proven experimentally and numerically for the considered system. To do so, three different loading cases (I, II and III) are compared. In case I, both waves X_ω and X_Ω act simultaneously on the specimen. LF excitation X_Ω varies harmonically between the values $F_1 = F_{min}$ and $F_2 = F_{max}$ (compare figure 3.1c). In case II, the specimen is loaded statically with F_{min} and harmonically with X_ω. In case III, the specimen is loaded statically with F_{max} and harmonically with X_ω. The experimental results are compared in figure 4.3. These experimental measurements were carried out on an aluminum specimen after 95% of its fatigue lifetime, when a fatigue crack was visible to the bare eye already. Note that modulation in this state does not only result from the crack, but also from other non-damage-induced nonlinearities in the system.

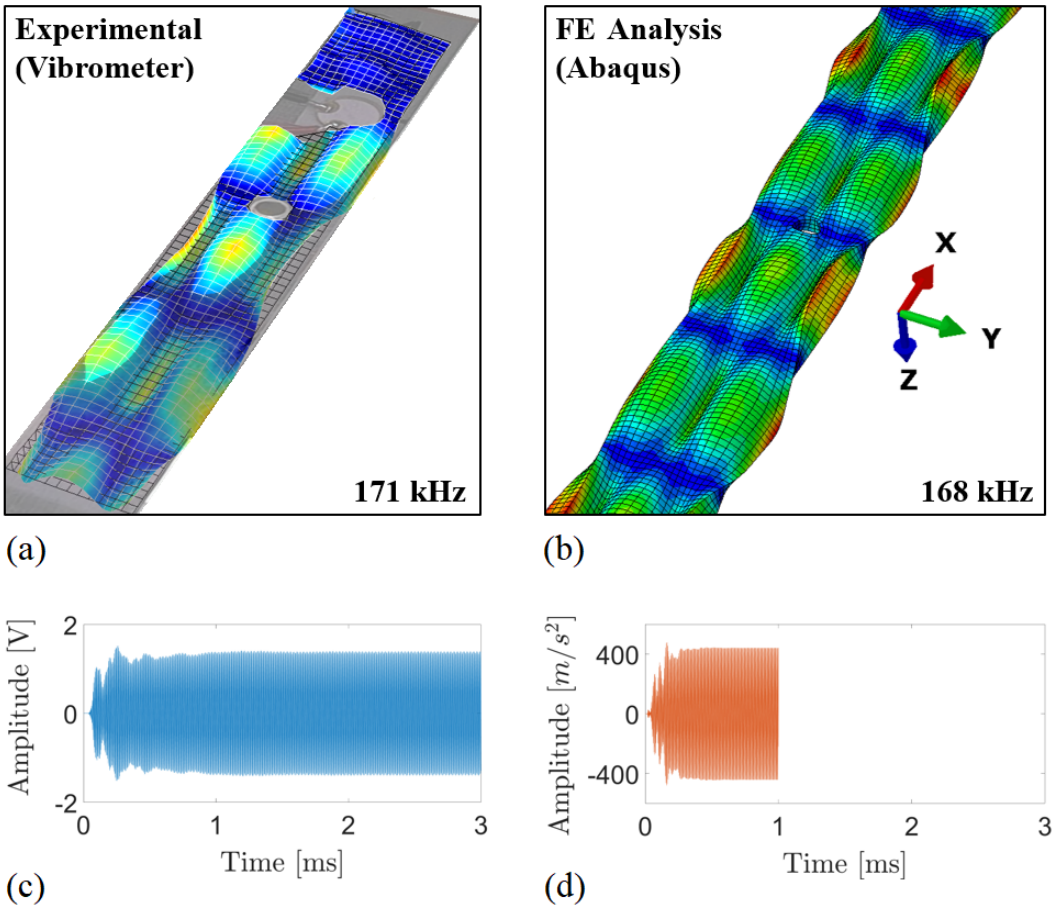

FIGURE 4.2: (a) Mode shape for natural frequency $\omega_{D,exp} = 171kHz \cdot 2\pi$ from an experimental modal analysis with a laser vibrometer (b) (Same) mode shape for natural frequency $\omega_{D,num} = 168kHz \cdot 2\pi$ from a numerical modal analysis with Abaqus CAE (c) Experimental system response over $3ms$ caused by ultrasonic excitation X_ω with $\omega = 170kHz \cdot 2\pi$ (d) Numerical system response (acceleration in out-of-plane direction Z) at the sensing node over $3ms$ caused by ultrasonic excitation X_ω with $\omega = 170kHz \cdot 2\pi$

Figure 4.3a shows the (highpass-filtered) system response of case I over time where $\omega = 213.4kHz \cdot 2\pi$. In figure 4.3b, the envelope function of that measurement is plotted (blue thin solid line). Additionally, the envelope functions for the corresponding cases II (red thick dashed line) and III (green thick solid line) are plotted in the same graph in figure 4.3b. Cases II and III show constant envelope functions, as expected. Note that the constant amplitudes from the static cases II and III are rather identical with the minimum and maximum amplitude values of the envelope function of case I. This experimental result demonstrates that the major assumption for the physical explanation, suggested in section 3.1, is valid for this setup. The error made by evaluating the steady-state response is $< 1\%$ and therefore negligible.

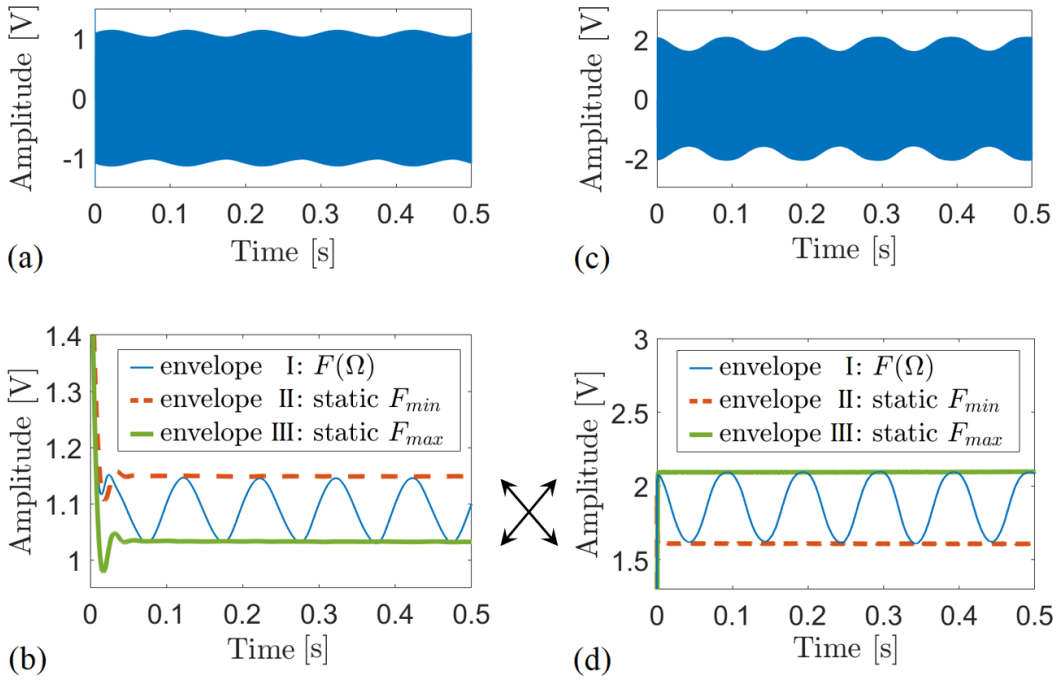

FIGURE 4.3: Experimental validation of the physical explanation: (a) Experimental system response for case I over 0.5s, $\omega = 213.4kHz \cdot 2\pi$, $\Omega = 10Hz \cdot 2\pi$ (b) Experimental envelope functions: case I from above (blue thin solid line); case II (red thick dashed line); case III (green thick solid line) (c) Experimental system response for case I over 0.5s, $\omega = 193kHz \cdot 2\pi$, $\Omega = 10Hz \cdot 2\pi$ (d) Experimental envelope functions: case I from above (blue thin solid line); case II (red thick dashed line); case III (green thick solid line)

When changing the excitation frequency to $\omega = 193kHz \cdot 2\pi$ a similar experimental result is found (figures 4.3c and 4.3d). Also in this case, the error is $< 1\%$. However, figure 4.3d shows that the tensile load F_{max} (case III) coincides with the maximum amplitude in the system response of case I. In figure 4.3b the opposite was the case: Tensile load F_{max} (case III) coincides with the minimum amplitude in the system response of case I. This finding is addressed and fully answered in section 5.2 using the suggested physical explanation.

The cases I, II and III were also simulated numerically. The results are shown in figure 4.4 for an excitation frequency $\omega = 199kHz \cdot 2\pi$. Figure 4.4a shows case I while figures 4.4b and 4.4c show the corresponding cases II and III. In the top graphs, the prescribed displacement in X-direction is plotted over time, representing the LF excitation X_Ω in figure 4.4a, and static tensile loading in figures 4.4b and 4.4c. In the bottom graphs, the system responses (acceleration in Z-direction at the sensing node) are plotted over time.

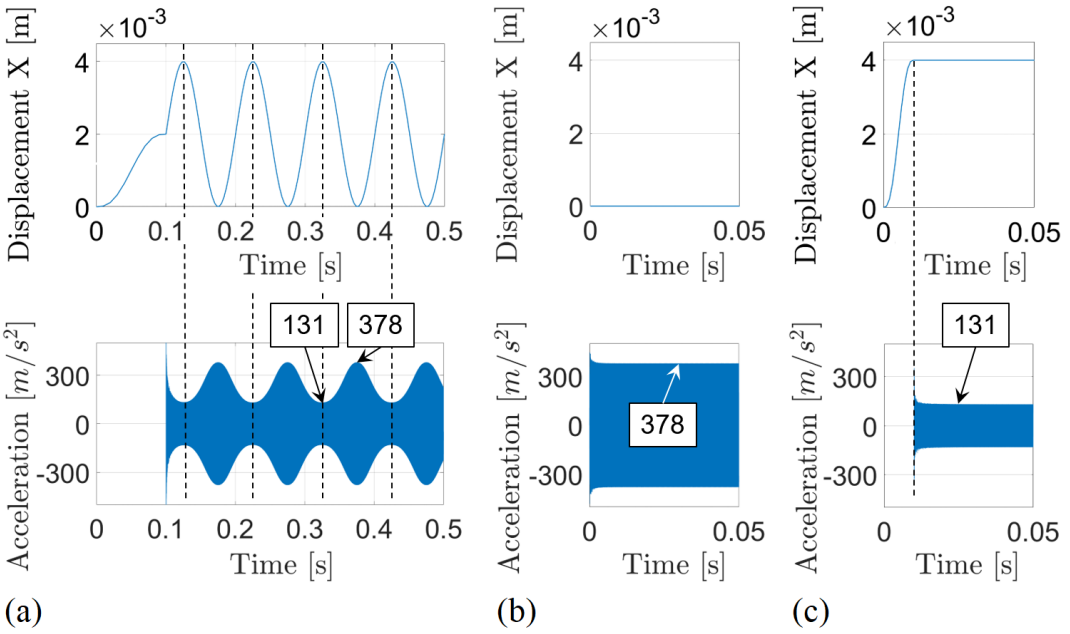

FIGURE 4.4: Numerical validation with $\omega = 199kHz \cdot 2\pi$ (a) Case I: X_Ω as prescribed displacement in X-direction over time with $\Omega = 10Hz \cdot 2\pi$ (top) and system response as Z-acceleration at the sensing node (bottom) (b) Case II: static F_{min} (top) system response (bottom) (c) Case III: static F_{max} (top) and system response (bottom) [19]

Note that in the FE model all material behaves linearly-elastic and there is no damage present. However, the system response at the bottom of figure 4.4a shows AM. This non-damage-induced modulation is caused by the variation of geometric stiffness[1] [11]: The application of a tensile force on a structure generates geometric bending stiffness that accumulates with the elastic bending stiffness EI (where E is the Young's modulus and I the second moment of inertia). Tensile stress in X-direction of the investigated aluminum specimen activates restoring forces in Z-direction as soon as bending is applied. The excitation of the LF wave X_Ω changes the present tensile stress in X-direction in the aluminum specimen periodically with $\Omega = 10Hz \cdot 2\pi$. Consequently, due to the geometric stiffness component, the total bending stiffness of the structure is varied accordingly. Considering the explanation in chapter 3 this necessarily causes AM and PM. Musicians utilize geometric stiffness to tune instruments such as pianos, violins and guitars.

[1]Note that the surface displacements in Z-direction reach amplitudes of only $\Delta u_{Z,num} = 2 \cdot 10^{-7} mm$ in this simulation. Since that is magnitudes smaller compared to the specimen's thickness ($t = 3mm$) other nonlinear geometric effects cannot have a significant impact on the ultrasonic vibration here. Also for the experimental setup investigated in this dissertation the author is certain that displacements $\Delta u_{Z,exp} << t = 3mm$. Measurements with a laser vibrometer reveal surface amplitudes with magnitudes of $\Delta u_{Z,exp} = 6 \cdot 10^{-6} mm$.

In order to make the non-damage-induced AM clearly visible here, the amplitude of the LF excitation X_Ω was scaled artificially with factor 20 compared to the amplitude in the experimental analysis ($A_{\Omega,num} = 20 \cdot A_{\Omega,exp}$).

Comparison of these three numerical cases I, II and III confirms the prior experimental results, since the constant amplitudes in the system responses of the static cases II and III match exactly the maximum and minimum amplitudes of the envelope function of the system response in case I, as shown in figures 4.4b and 4.4c, respectively. The tensile load F_{max} (case III) coincides with the minimum amplitude in the system response of case I here.

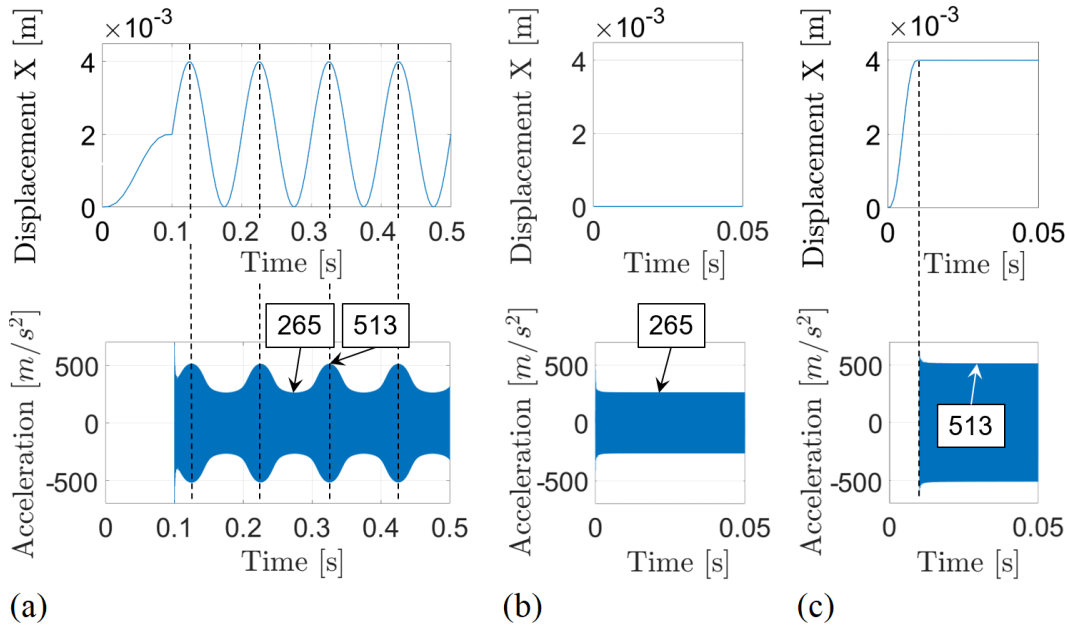

FIGURE 4.5: Numerical validation with $\omega = 205kHz \cdot 2\pi$: (a) Case I: X_Ω as prescribed displacement in X-direction over time with $\Omega = 10Hz \cdot 2\pi$ (top) and system response as Z-acceleration at the sensing node (bottom) (b) Case II: static F_{min} (top) and system response (bottom) (c) Case III: static F_{max} (top) and system response (bottom) [19]

When changing the excitation frequency ω in the numerical analysis to $\omega = 205kHz \cdot 2\pi$, the opposite case was found (figure 4.5): The tensile load F_{max} (case III) coincides with the maximum amplitude in the system response of case I. This phenomenon is addressed and explained in section 5.2.

4.3 Limits of the explanation's applicability

The physical explanation is—in principle—applicable to any dynamic system. However, the accuracy of its results depends on the fulfillment of its underlying major assumption: It is assumed that the ultrasonic excitation X_ω

causes a steady-state vibration (amplitude and phase constant over time) before the LF excitation X_Ω can change the system significantly. Therefore, a deviation from the latter circumstance will limit the explanation's applicability. The author can think of two relevant parameters that can cause such a deviation: The size of the system and the frequency ratio ω/Ω. Increasing the system size will lengthen the ultrasonic propagation (and reflection) paths and consequently prolong the amount of time needed to reach a steady-state vibration. The decrease of the frequency ratio ω/Ω will affect the fulfillment of the assumption in the same manner. Both described deviations will worsen the accuracy: The error—made by evaluating the steady-state responses—increases.

Regarding the system size, note that most metal sheets prone to fatigue damage in civil engineering are held by stiffeners in short intervals to prevent buckling. Such stiffeners resemble fixed boundary conditions regarding a potential VAM application and limit the system size "naturally". Even for a large plate without natural boundaries, one could fix boundary conditions temporarily in order to evaluate the integrity of the steel sheet.

Regarding the frequencies, note that it is the user who chooses Ω and ω for application and hereby determines the ratio ω/Ω. As discussed in section 4.2 and demonstrated in figure 4.4, the error made by evaluating the steady-state responses for the investigated aluminum specimen and the frequency ratio $\omega/\Omega = 19900$ is less than 1%. The error is calculated according to equation 4.1.

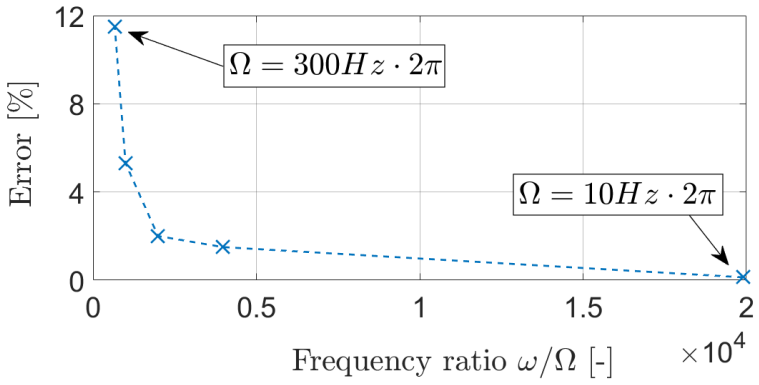

FIGURE 4.6: The error (made by evaluating the steady-state responses instead of the modulated dynamic response) is plotted over the frequency ratio ω/Ω for the investigated aluminum specimen. The crosses indicate numerical results. The dotted line represents linear interpolation.

$$Error = \left| \frac{A_{stat} - A_{dyn}}{A_{dyn}} \right| \cdot 100\% \tag{4.1}$$

A_{dyn} is the maximum or minimum amplitude in the modulated system response according to the dynamic loading case I while A_{stat} is the respective steady-state amplitude according to the static loading cases II and III.

Figure 4.6 shows the dependency of the error in % on the ratio ω/Ω for the investigated aluminum specimen. The plotted data results from FE simulations with different LF vibration frequencies Ω in the range $10Hz \cdot 2\pi \leq \Omega \leq 300Hz \cdot 2\pi$ while the ultrasonic frequency $\omega = 199kHz \cdot 2\pi$ and all other settings remain the same.

Chapter 5

Findings based on the explanation

This chapter presents five analytical findings that are derived directly from the physical explanation in chapter 3. Most of them are demonstrated experimentally and numerically. Note that the content in this chapter was partially published by Dorendorf et al. in [19].

5.1 Coexistence of amplitude modulation and phase modulation

The physical explanation suggests that AM and PM both result from a quasi-static variation of the natural frequency $\omega_D(\Omega)$. It can be concluded that any nonlinearity that does vary ω_D causes both modulation types—AM and PM. The experimental and numerical results in the scope of this dissertation confirm this.

Figure 5.1 shows the observed PM in the experimental data that has been presented in figure 4.3c previously. To visualize PM here, the system response (blue graph) is plotted against the ultrasonic excitation with $\omega = 193kHz \cdot 2\pi$ (red graph) over $0.5s$ in figure 5.1a. Figures 5.1b and 5.1c show the phases $\theta_1 = +0.12\pi$ and $\theta_2 = +0.21\pi$ of the system response at $t_1 = 0.295s$ and $t_2 = 0.345s$, respectively. The difference $\Delta\theta = |\theta_1 - \theta_2| = 0.09\pi$ indicates the extent of PM here.

Also the numerical results show corresponding PM. Figure 5.2 refers to the same numerical system response that was given in figure 4.4a. In figure 5.2a this system response (blue line) is plotted against the ultrasonic excitation with $\omega = 199kHz \cdot 2\pi$ (red line). Figures 5.2b and 5.2c show the phases $\theta_1 = -0.31\pi$ and $\theta_2 = +0.27\pi$ of the system response at $t_1 = 0.275s$ and $t_2 = 0.325s$, respectively. Again, the difference $\Delta\theta = |\theta_1 - \theta_2| = 0.58\pi$ indicates the extent of PM.

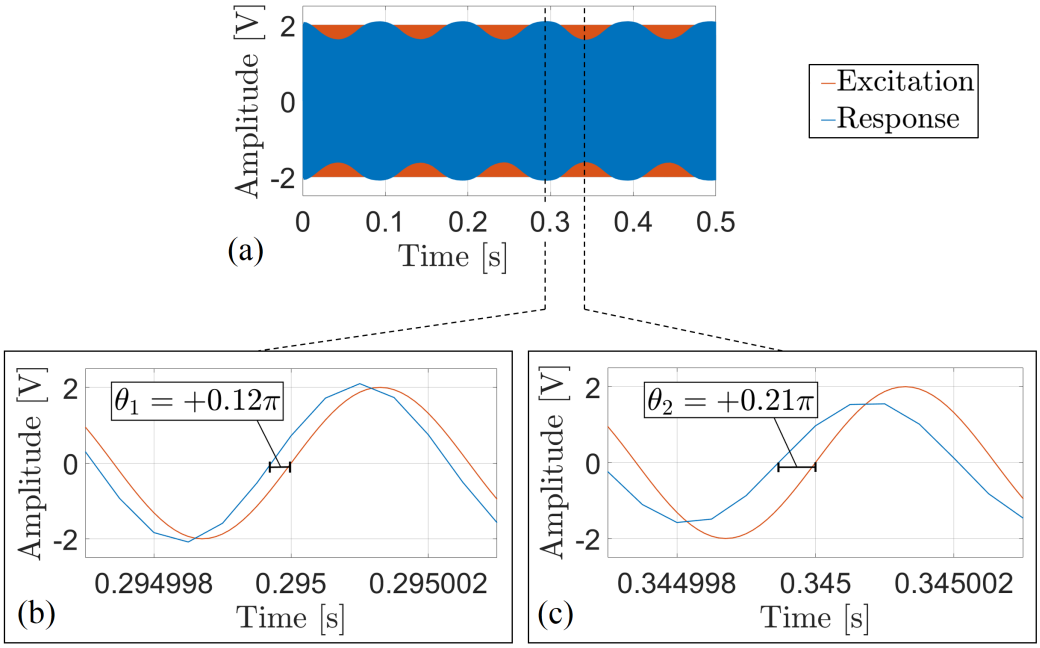

FIGURE 5.1: Experimental system response in Volt (blue) vs. ultrasonic excitation X_ω with $\omega = 193kHz \cdot 2\pi$ (red): (a) Over $0.5s$ (b) Close-up at $t_1 = 0.295s$ (c) Close-up at $t_2 = 0.345s$ [19]

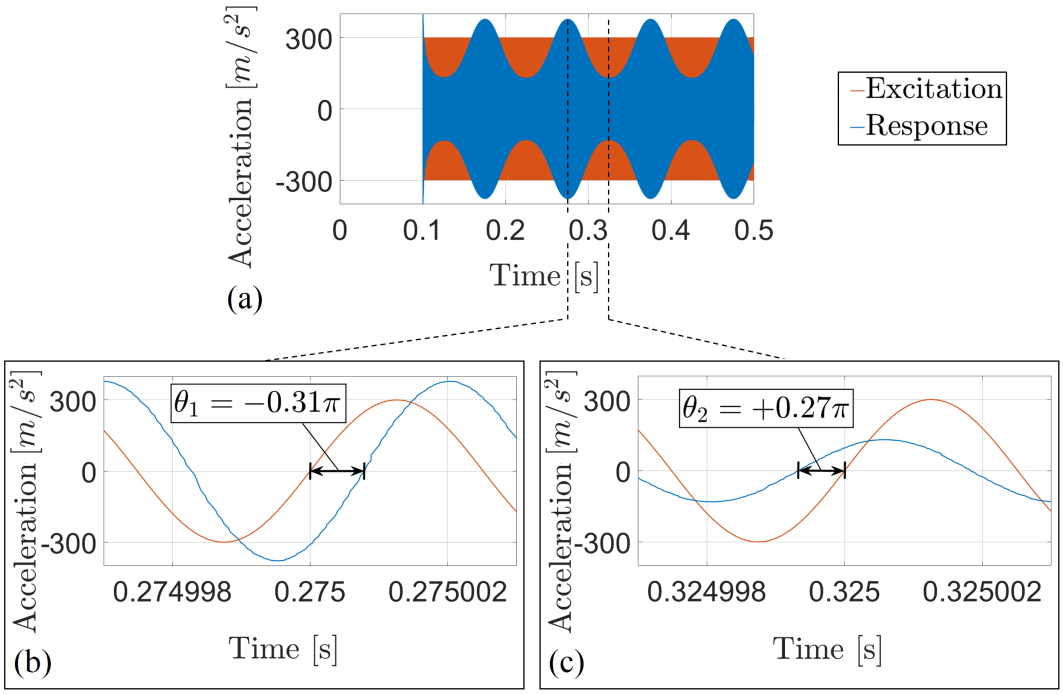

FIGURE 5.2: Numerical system response in m/s^2 (blue) vs. ultrasonic excitation X_ω with $\omega = 199kHz \cdot 2\pi$ (red): (a) Over $0.5s$ (b) Close-up at $t_1 = 0.275s$ (c) Close-up at $t_2 = 0.325s$

The validation of the major assumption was proven to be true in section 4.2 by demonstrating that the envelope describing the AM matches the steady-state amplitudes of the respective static cases. PM is less vivid to the bare eye compared to AM. Nevertheless, note that it can be shown analogously here that the minimum and maximum phases in the modulated system response match the respective phases in the static simulations.

As reviewed in section 2.2 there have been ambitions in the scientific community to exploit PM instead of AM for damage detection [14, 18, 27, 42]. Donskoy et al. indicated the hypothesis in 2018 [14] that initial fatigue damage may primarily cause PM. Note that on the basis of the suggested physical explanation in this dissertation there is no reason to believe that any specific nonlinearity causes primarily AM or PM. The latter statement complies with the work that Oppermann et al. (including the author of this dissertation) presented in 2021 [49].

5.2 Temporal coincidence of the envelope and the loading state

In the most popular review paper on VAM [53] it is indicated that the maximum tensile load due to the LF excitation X_Ω is expected to coincide with the minimum amplitude of the ultrasonic system response. This understanding complies with other literature as discussed in section 2.2.

Contrarily, the experimental results in figure 4.3 demonstrate that the tensile load F_{max} can either coincide with the minimum amplitude in the system response or the maximum amplitude in the system response, depending on excitation frequency ω. Comparison of the numerical results in figure 4.4 and figure 4.5 confirms this finding.

When considering the suggested physical explanation and the analytical solution for the amplitude in the steady-state response, both cases must necessarily exist, because the choice of excitation frequency ω can cause $\beta(\Omega)$ to range above or below the value 1.0. Both cases ($\beta_{min} < \beta_{max} < 1.0$ and $1.0 < \beta_{min} < \beta_{max}$) are indicated in figure 5.3. They necessarily lead to opposite results, as described above.

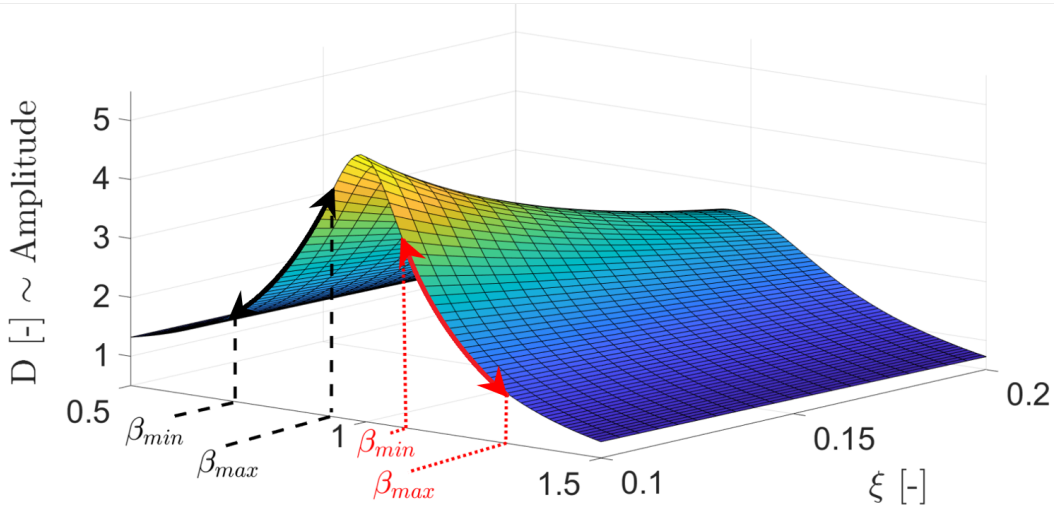

FIGURE 5.3: Dynamic magnification factor D (proportional to the amplitude) for the steady-state response over ratio $\beta = \omega/\omega_0$ and damping ratio ξ. The range of β will affect wether the tensile loading F_{max} coincides with the minimum or maximum amplitude in the system response. [19]

5.3 Variety of envelope functions

The previous finding is taken one step further: Besides the two cases of (contrary) sine-like envelope functions, envelope functions of different shape can be found experimentally and numerically by varying the excitation frequency ω. All of them are consistent with the suggested physical explanation.

In figure 5.4 one of those differently looking envelopes is shown and explained. The plot in figure 5.4a shows an experimentally measured system response over $0.5s$ with $\omega = 209.6kHz \cdot 2\pi$ and $\Omega = 10Hz \cdot 2\pi$. A comparable envelope function is found numerically for $\omega = 201kHz \cdot 2\pi$ and $\Omega = 10Hz \cdot 2\pi$ and is plotted over $0.5s$ in figure 5.4b. Considering the suggested explanation for AM this envelope function is expected for $\beta_{min} < 1.0 < \beta_{max}$ (figure 5.4c). The steady-state amplitudes A and B corresponding to β_{min} and β_{max} differ in their values significantly ($A > B$).

Figure 5.5 shows another characteristic envelope function. Again, an experimental system response is plotted in 5.5a, while a numerical system response is plotted in 5.5b. As in the previous case, also this is explainable in the range $\beta_{min} < 1.0 < \beta_{max}$ (figure 5.5c). The envelope function appears to look like a $20Hz$-sine. However, this is only due to the fact that the system response reaches similar amplitude values in the points A and B ($A \approx B$).

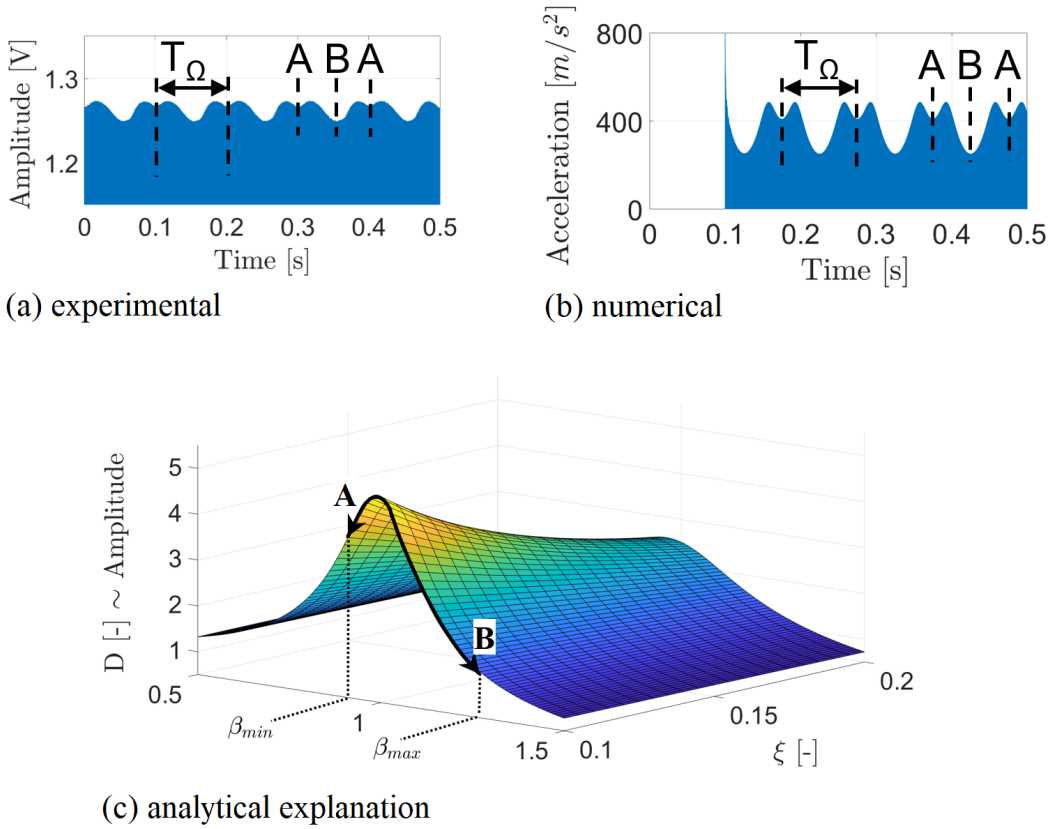

(a) experimental

(b) numerical

(c) analytical explanation

FIGURE 5.4: (a) Experimental system response over time, $\omega = 209.6kHz \cdot 2\pi$ and $\Omega = 10Hz \cdot 2\pi$ (b) Numerical system response at the sensing node over time, $\omega = 201kHz \cdot 2\pi$ and $\Omega = 10Hz \cdot 2\pi$ (c) Analytical solution for the amplitude in the steady-state response: The variation between β_{min} and β_{max} with frequency Ω explains the envelope functions above. [19]

The last type of envelope function found experimentally and numerically is shown in figure 5.6. Note that all previous envelope functions were explained by taking into account the contribution of one single natural frequency and its corresponding mode shape only. To explain the envelope functions in figure 5.6a (experimental result) and 5.6b (numerical result) the contribution of two neighboring natural frequencies and their corresponding mode shapes to the system response have to be considered. When plotting the dynamic magnification factor D for a two-degree-of-freedom system over the excitation frequency ω (not over the ratio β) and the damping ratio ξ one derives two peaks (one for each natural frequency). Such a function is plotted schematically in figure 5.6c. When the amplitude of the system response varies between the indicated values A and B with frequency Ω, envelope functions as plotted in figures 5.6a and 5.6b are expected.

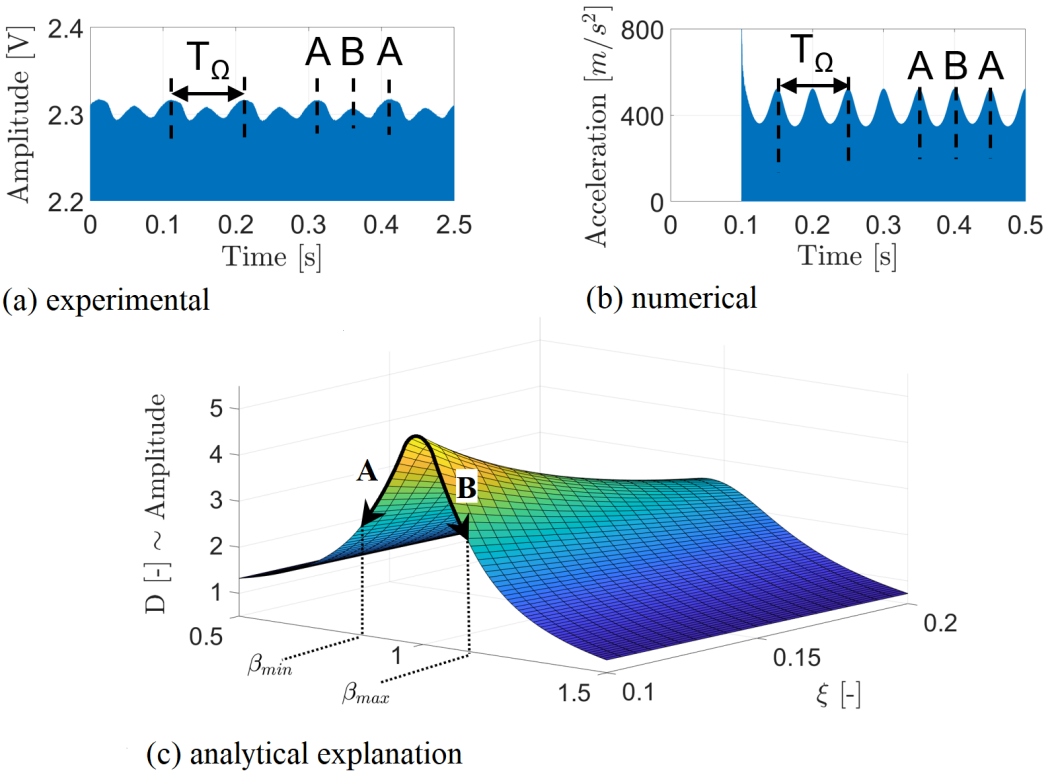

FIGURE 5.5: (a) Experimental system response over time, $\omega = 203.3kHz \cdot 2\pi$ and $\Omega = 10Hz \cdot 2\pi$ (b) Numerical system response at the sensing node over time, $\omega = 202kHz \cdot 2\pi$ and $\Omega = 10Hz \cdot 2\pi$ (c) Analytical solution for the amplitude in the steady-state response: The variation between β_{min} and β_{max} with frequency Ω explains the envelope functions above. [19]

5.4 Nonlinearities causing contrary modulations

Now, consider two nonlinearities that both exhibit nonlinear-elastic behavior and each of them causes modulation with a sine-like envelope. However, these two nonlinearities work in opposite directions: While one nonlinearity stiffens the system under tensile loading, the other nonlinearity softens it. What happens if these two nonlinearities were combined in the same system? When considering the suggested physical explanation it has to be concluded that the natural frequency $\omega_D(\Omega)$ will be varied in opposite directions. Hence, the steady-state amplitude and the steady-state phase will be affected in a contrary manner. For the theoretical case that the nonlinearities (and respective modulations) are equally strong, the modulations could neutralize each other and result in a system response that is not modulated at all. In the author's opinion this finding is highly relevant due to the following background: Most VAM studies in the literature measure a baseline modulation at a time when the structure is expected to be pristine [12, 16, 40].

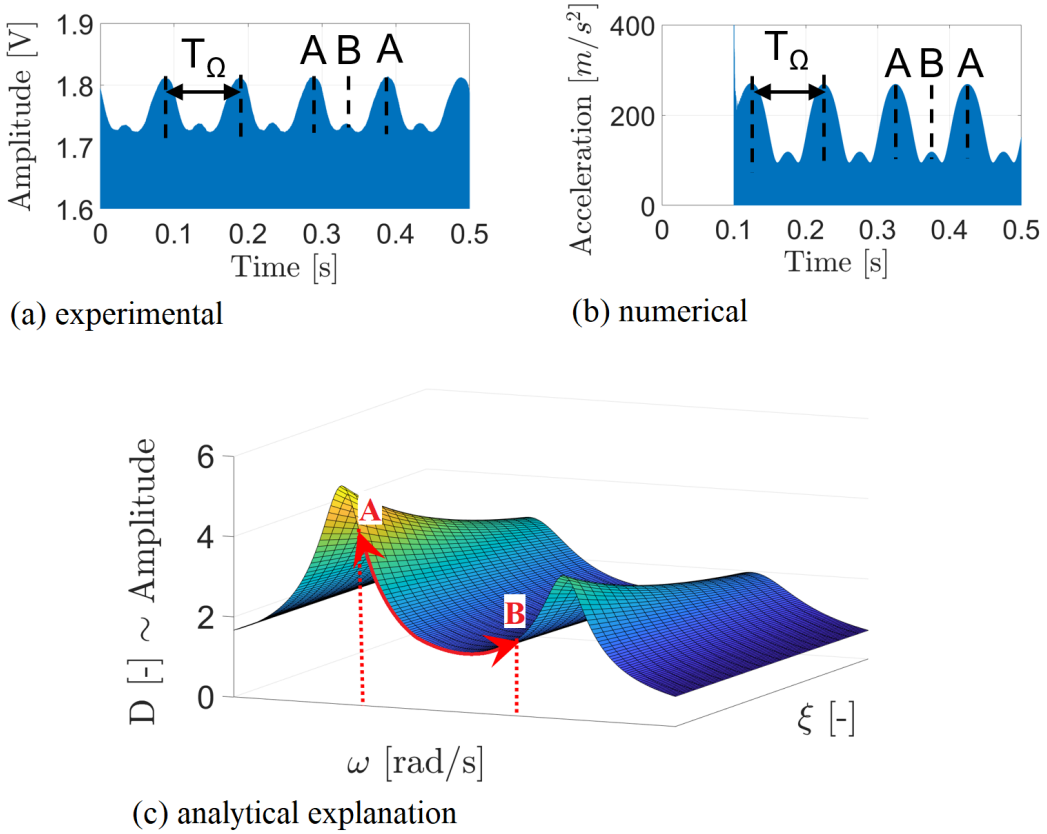

(a) experimental

(b) numerical

(c) analytical explanation

FIGURE 5.6: (a) Experimental system response over time, $\omega = 208.1kHz \cdot 2\pi$ and $\Omega = 10Hz \cdot 2\pi$ (b) Numerical system response at the sensing node over time, $\omega = 210kHz \cdot 2\pi$ and $\Omega = 10Hz \cdot 2\pi$ (c) Schematic analytical solution for the amplitude in the steady-state response for a two-degree-of-freedom system over excitation frequency ω and damping ratio ξ. By evaluating a two-degree-of-freedom system the contributions of two different mode shapes to the system response are considered. The variation between the values A and B with frequency Ω explains the envelope functions above. [19]

This baseline modulation is taken as a reference. Later, during the lifetime of the structure, the modulation is measured and compared to the reference. The initiation and growth of local damage is expected to increase the modulation in the global system response. Taking into account that nonlinearities may cause contrary modulations the conventional evaluation method appears prone to misleading conclusions. Chapter 6 takes a closer look at this finding: The behavior of three different nonlinearities present in the aluminum specimen are investigated separately. One of them—the variation of geometric stiffness—causes the system to stiffen under tensile loading. The

other two investigated nonlinearities—the nonlinear-elastic material behavior of aluminum and the contact of fatigue crack surfaces—exhibit nonlinearity in the opposite direction: They soften the system under tensile loading. In fact, it is demonstrated numerically in chapter 6 that these two do cause AM in the system response that works contrarily to the modulation resulting from the geometric stiffness variation.

5.5 VAM applications without the low frequency vibration

It was demonstrated in section 4.2 that the minimum and maximum amplitudes in the modulated system response match the respective steady-state amplitudes under static loading. Consider figure 4.4 once again. The system response in figure 4.4a shows a sine-like envelope. The author calls it "sine-like" here, because it does show one minimum and one maximum per period $T_\Omega = 0.1s$. When taking a closer look however, one realizes that the shape differs from an actual sine, because the minimum and maximum are not shaped symmetrically. Why is this relevant? In case the shape of the envelope function was known in a qualitative manner, one could artificially compute the modulated system response on the basis of the two steady-state amplitudes in figures 4.4b and 4.4c. Note that the steady-state amplitudes can be measured for the considered aluminum specimen within $\Delta t = 0.001s$ each as demonstrated in figure 4.2. When measuring the modulated system response for a VAM application one necessarily has to measure for at least a full period of LF vibration X_Ω which is $T_\Omega = 0.1s$ here. It can be concluded that measuring two steady-state responses instead of the modulated one would reduce the measurement time and the corresponding data by 98%. From a practical perspective there is more benefits to this approach: There is no need to excite the LF vibration X_Ω in order to apply VAM to a real-world structure. The idea is exploited and discussed by Boll et al. (including the author of this dissertation) in 2023 [5].

Chapter 6

Separation and quantification of nonlinearities

6.1 Motivation

The goal of VAM applications is to evaluate the integrity of a structure by the present modulation in the system response. One major challenge jeopardizing the success of this approach is the following: Any nonlinearity in the system may cause modulation—not only structural damage[1].

In order to make VAM applications robust and reliable it is necessary to understand all nonlinearities in the system of interest and the extent of modulation they can cause. Therefore, this chapter investigates three nonlinearities in the same system separately:

(1) variation of the geometric stiffness (global, non-damage-induced)
(2) nonlinear-elastic behavior of aluminum (global, non-damage-induced)
(3) contact of fatigue crack surfaces (local, damage-induced)

Why do these nonlinearities cause modulation under tensile fatigue loading? How can one approach quantifying the modulation caused by them individually? Does the modulation accumulate when evaluating the conventional MI for damage monitoring? These are the questions this chapter aims to answer.

[1] Most VAM studies measure a baseline modulation at a time when the structure is expected to be pristine. This baseline modulation is taken as a reference. Later, during the lifetime of the structure, the modulation is measured and compared to the reference. The initiation and growth of local damage is expected to increase the modulation in the global system response. This procedure relies on two assumptions: First, all known and unknown nonlinearities that cause the baseline modulation are expected not to change over time. Second, it is expected that the nonlinear behavior of developing structural damage causes additional modulation that accumulates with the reference.

It is very difficult—if not impossible—to separate the three nonlinearities above and the modulation they cause in an experimental setup. Therefore, the nonlinearities and their contributions to the system response are investigated numerically with explicit dynamic simulations in Abaqus CAE. The great advantage of a FE analysis is that the user controls all input data and can hereby artificially suppress features that are present in reality. The investigated system is the same aluminum specimen considered previously in this dissertation. Note that nonlinearities (1) and (2) are global nonlinearities since they are distributed over the entire structure while (3) is a local nonlinearity.

6.2 Variation of the geometric stiffness

The application of a tensile force on a structure increases its bending stiffness. As introduced in section 4.2, this effect is called geometric stiffness [11]. The excitation of X_Ω in the structure varies the tensile force harmonically with low frequency Ω. Consequently, the geometric stiffness varies harmonically with Ω directly affecting the natural frequencies of the system. Taking into account the physical explanation from chapter 3 this necessarily leads to AM and PM in the system response. To quantify the modulation caused by this nonlinearity for a realistic setup a simulation is run that is quite similar to the ones from chapters 4 and 5. The meshed specimen is shown in figure 6.1.

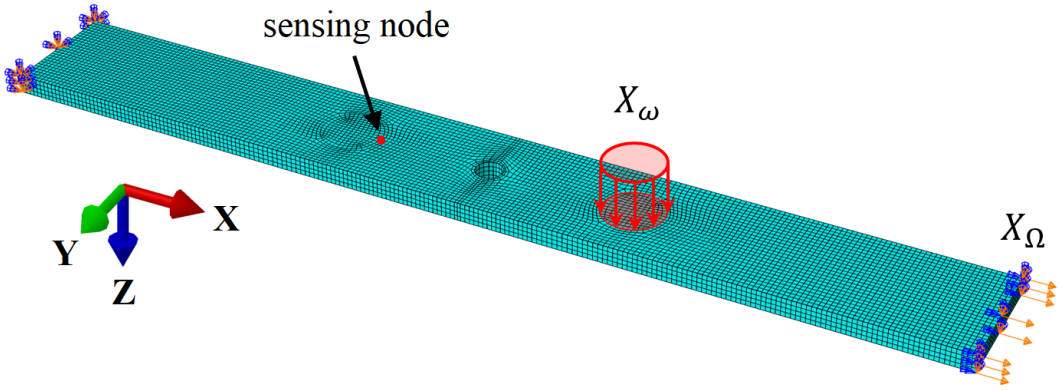

FIGURE 6.1: FE model of the specimen with dimensions $160mm/20mm/3mm$: LF excitation X_Ω, ultrasonic excitation X_ω, the system response is measured at the sensing node

Compared to previous simulations the mesh size was reduced to $0.75mm$, the Youngs' modulus was increased to $E = 7300kN/cm^2$ (linear-elastic behavior, Poisson's lateral strain $\nu = 0.296$) and the amplitude of the LF excitation was reduced to a realistic value of $A_\Omega = 0.2mm$. The elongation of $\Delta l = 0.2mm$ causes a strain of $\epsilon_X = 0.00125$. This strain (1,25‰) lies in the elastic range of aluminum. The excitation frequencies are $\omega = 199kHz \cdot 2\pi$ and $\Omega = 10Hz \cdot 2\pi$. The damping ratio is set to $\xi = 0.01$ for the frequency range of interest (Rayleigh damping coefficients: $\alpha_R = 80$, $\beta_R = 1.38 \cdot 10^{-8}$).

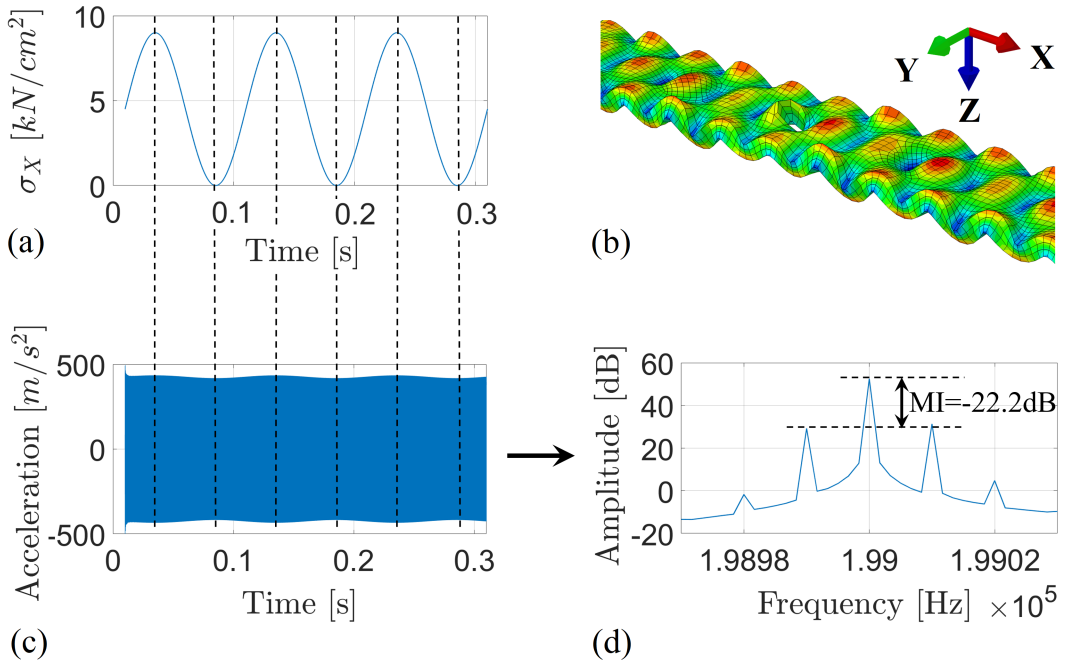

FIGURE 6.2: Results from the simulation with only one nonlinearity present: The variation of geometric stiffness (a) Stress σ_X over $0.3s$ at an element in the sensing node's direct vicinity (b) Coordinate system for orientation; deformation of the specimen is magnified by factor $2.5 \cdot 10^7$ (c) Acceleration in Z-direction at the sensing node over time (system response) (d) FFT spectrum corresponding to the system response

Figure 6.2 shows the results from the simulation in which the only present nonlinearity is (1) the variation of geometric stiffness. All material in the model behaves linearly-elastic. On top, in figure 6.2a, the stress σ_X (in X-direction) for an element in the sensing node's direct vicinity is plotted over $0.3s$. It represents the LF excitation X_Ω[2]. The coordinate system and the FE model are visualized in figure 6.2b. Note that the shown deformation of the

[2]Also the ultrasonic excitation X_ω varies the stress σ_X at this element with frequency $\omega = 199kHz \cdot 2\pi$. The amplitude of this stress variation is only $\Delta\sigma_X = 0.1kN/cm^2$ though and therefore not visible in this plot. Note that the excitation amplitudes differ significantly ($A_\omega << A_\Omega$).

specimen in this image is magnified by the factor $2.5 \cdot 10^7$ to make the ultrasonic vibration visible here. In figure 6.2c the acceleration in Z-direction at the sensing node is plotted over $0.3s$. This acceleration is considered as the system response for latter comparisons. Figure 6.2d shows the FFT spectrum of the system response in dB. The MI is the most common parameter to quantify the modulation in the literature. It reaches a value of $MI = -22.2dB$ here. Note that this "quantified" modulation is the result at one specific node in this FE mesh. Looking at the system response at a different node, changing the excitation frequency ω or changing the amplitude A_Ω can change this quantified value significantly. In the following sections 6.3 and 6.4 more simulations are carried out with additional nonlinearities present in the system. The excitation frequencies and amplitudes are identical and the system responses are measured at the same node to provide the most accurate comparison possible. However, it has to be clear that these quantified results are not valid in general. The goal of this chapter is to explain why and how these nonlinearities cause modulation and to present approaches that enable their quantification for specific circumstances.

6.3 Nonlinear-elastic behavior of aluminum

Within the elastic range of their behavior metals show a nearly linear stress-strain dependency under tension. A linear approximation is sufficiently accurate for most engineering tasks and is the basis for using Hooke's law and the Young's modulus E [28].

When taking a closer look at tensile test data for aluminum however, one realizes that the material does not behave perfectly linear in its elastic range. Five tensile tests are performed with aluminum alloy EN-AW6060 specimens according to German design code DIN 50125:2016-12 [59]. The specimens' dog-bone geometry is shown in figure 6.3a with dimensions in mm. It's a flat dog-bone specimen with thickness $t = 8mm$ (figure 6.3b). Figure 6.3c shows a representative stress-strain curve from one of the five tensile tests.

The stress-strain curve shows yielding at roughly $\epsilon = 3‰$ initializing plastic material behavior. In the elastic range of the material ($\epsilon < 3‰$) the relationship appears to be linear to the bare eye. A close-up of the test data for $0 < \epsilon < 0.0025$ is presented in figure 6.3d. Comparison of the test data (blue solid curve) with a linear reference (red dashed line) demonstrates the weak—but present—nonlinearity of the elastic stress-strain dependency.

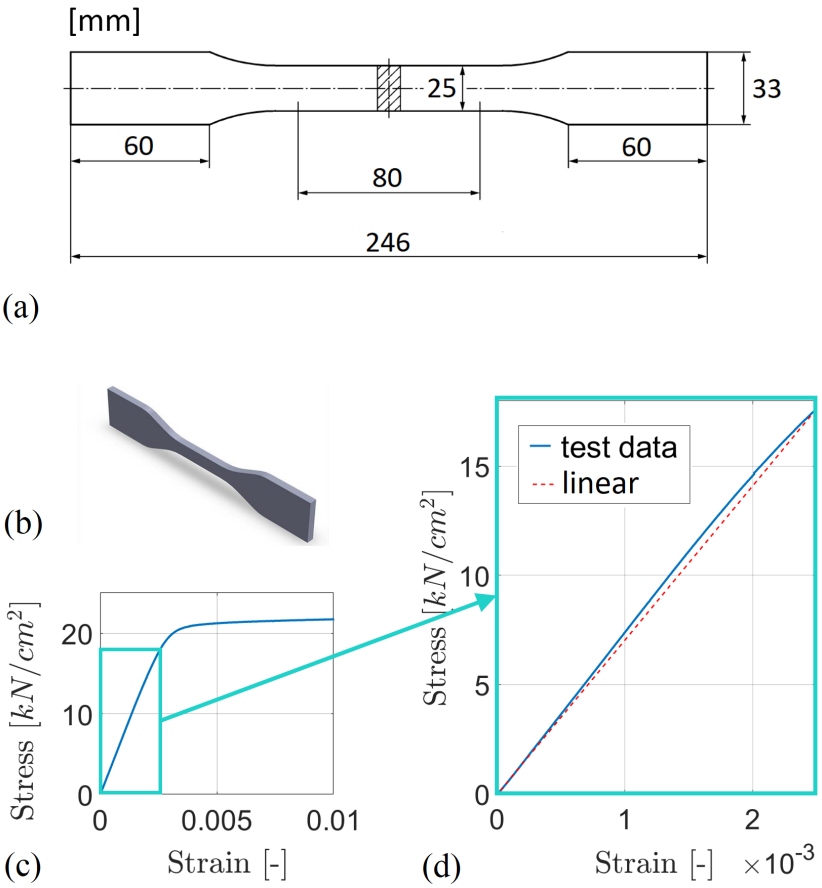

FIGURE 6.3: (a) In-plane geometry in mm (b) Flat dog-bone specimen with thickness $t = 8mm$ (c) Tensile stress-strain curve for aluminum alloy EN-AW6060 (AlMgSi0,5/3.3206) (d) Close-up of the tensile stress-strain curve (blue solid curve) with linear reference for comparison (red dashed line)

The test data in the range of $0 < \epsilon < 0.0025$ is used as input data to define a nonlinear-elastic material in Abaqus CAE[3]. In the following step, a dynamic explicit simulation is run that is identical to the one presented in section 6.2 with the only difference that the entire material in the model is defined with the weakly nonlinear-elastic data instead of the linear-elastic material. Note that the variation of geometric stiffness is not artificially suppressed in this second simulation and that therefore both nonlinearities—(1) the variation of geometric stiffness and (2) the nonlinear-elastic behavior of aluminum—are present here. The results of the two simulations are compared in figure 6.4. The stress state in closest vicinity of the sensing node is plotted in figure 6.4a and represents the LF excitation X_Ω. Figure 6.4b shows the global coordinate system in the FE model for orientation. In figure 6.4c the results from

[3]After a polynomial fit of the test data in MATLAB (common practice) the hyperelastic material model "Marlow" is used which follows the fitted uniaxial tensile test data exactly [56].

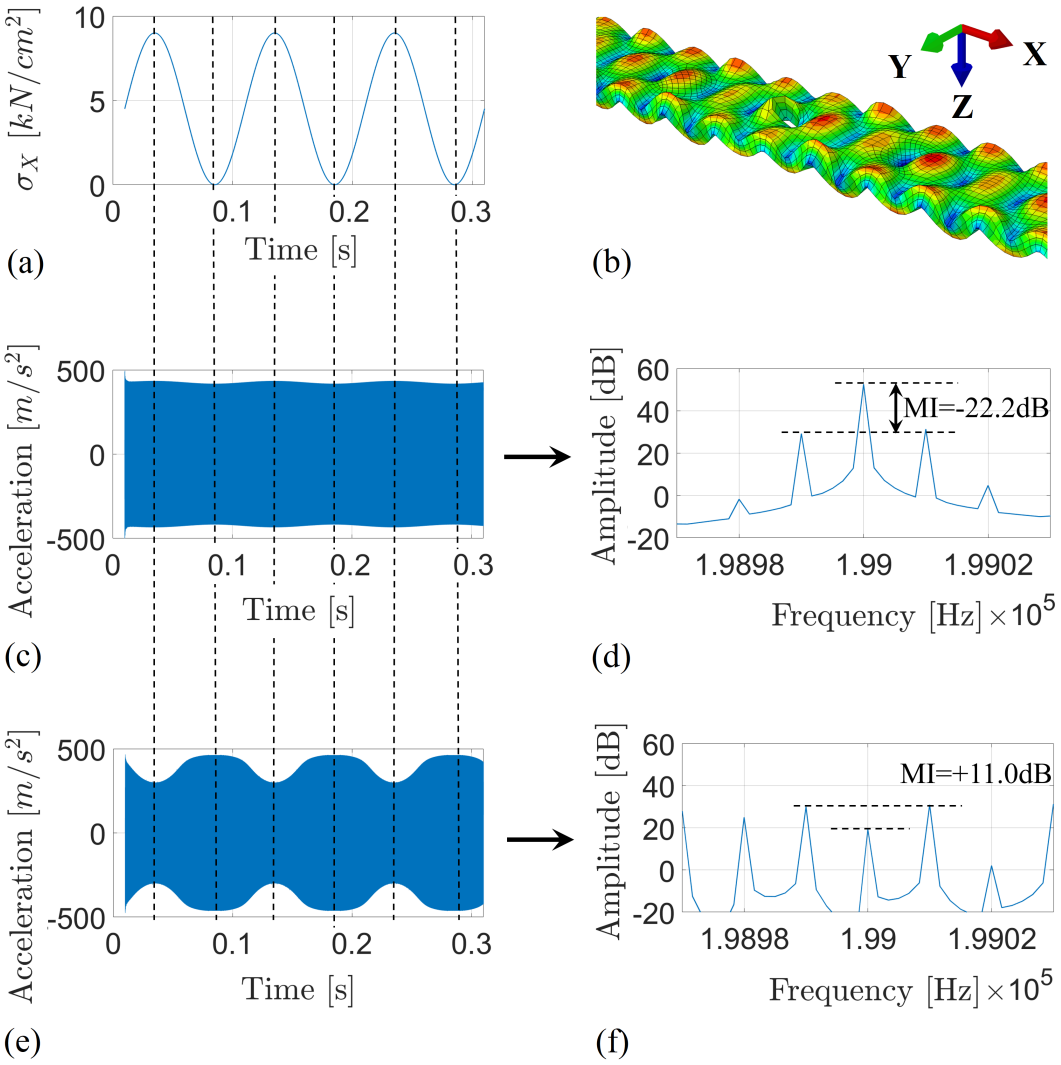

FIGURE 6.4: (a) Stress σ_X over time in direct vicinity of the sensing node (b) Coordinate system for orientation; deformation of the specimen is magnified by factor $2.5 \cdot 10^7$ (c) System response (acceleration in Z-direction) at the sensing node (the only present nonlinearity in this simulation is (1) the variation of geometric stiffness) (d) corresponding FFT spectrum in dB (e) System response (acceleration in Z-direction) at the sensing node (the present nonlinearities in this simulation are (1) the variation of geometric stiffness and (2) the nonlinear-elastic material behavior of aluminum) (f) Corresponding FFT spectrum in dB

the first simulation only governing (1) the variation of geometric stiffness are presented with the corresponding FFT spectrum in dB in figure 6.4d. The results from the second simulation—governing (1) the variation of geometric stiffness and (2) the nonlinear-elastic behavior of aluminum—are shown analogously in figure 6.4e (system response in time domain) and figure 6.4f (FFT spectrum). The comparison in time domain demonstrates that (2) the

nonlinear-elastic behavior of aluminum affects the system response significantly. Stronger AM can be observed by eye. The corresponding FFT spectrum shows that the first pair of sidebands at $\omega \pm \Omega = (199 \pm 0.01)kHz \cdot 2\pi$ has risen above the amplitude A_ω. Conventional quantification of the spectrum leads to $MI = +11.0dB$. It is significantly higher than in the previous simulation with an increase of $\Delta MI = 33.2dB$. The broader spectrum (not plotted here) shows up to one hundred pairs of sidebands at $\omega \pm n \cdot \Omega$ where $n \in \mathbb{N}$ for the second simulation.

Interestingly, the time domain comparison (figure 6.4c vs. 6.4e) reveals something that the corresponding spectra (and MIs) do not display: The modulation is not simply increased in the second simulation, the envelope function of the modulated system response is also reversed: The maximum of the envelope in figure 6.4c coincides with the minimum of the envelope in figure 6.4e. This result demonstrates the validity of the fourth analytical finding that was concluded from the physical explanation in section 5.4: Different nonlinearities combined in the same system can cause contrary modulations. According to the suggested physical explanation this phenomenon must necessarily exist: While nonlinearity (1) stiffens the system under tensile loading, nonlinearity (2) softens it. Consequently, the (dominating) natural frequency $\omega_0(\Omega)$ is varied in opposite directions. Hence, the steady-state amplitude and the steady-state phase are affected contrarily.

6.4 Contact of fatigue crack surfaces

It is intuitive why (1) the variation of geometric stiffness and (2) the nonlinear-elastic behavior of aluminum exhibit nonlinear-elastic behavior in a tensile fatigue loading scenario of the specimen. In the author's opinion it is less intuitive to understand why two rough crack surfaces which are opened and closed repetitively should exhibit nonlinear-elastic behavior under purely tensile fatigue loading.

However, the literature review in section 2.2 has shown that the latter is the common understanding in the scientific community. The most popular explanation in the literature is the nonlinear-elastic behavior due to Hertzian contact [12]. The controversy that has not been clearly addressed in the literature to the author's best knowledge is the following: The argument of Hertzian contact assumes pressure between the surfaces. Many VAM studies however report experimental work with purely tensile fatigue loading setups without clarifying why nonlinear-elastic behavior of the crack is expected.

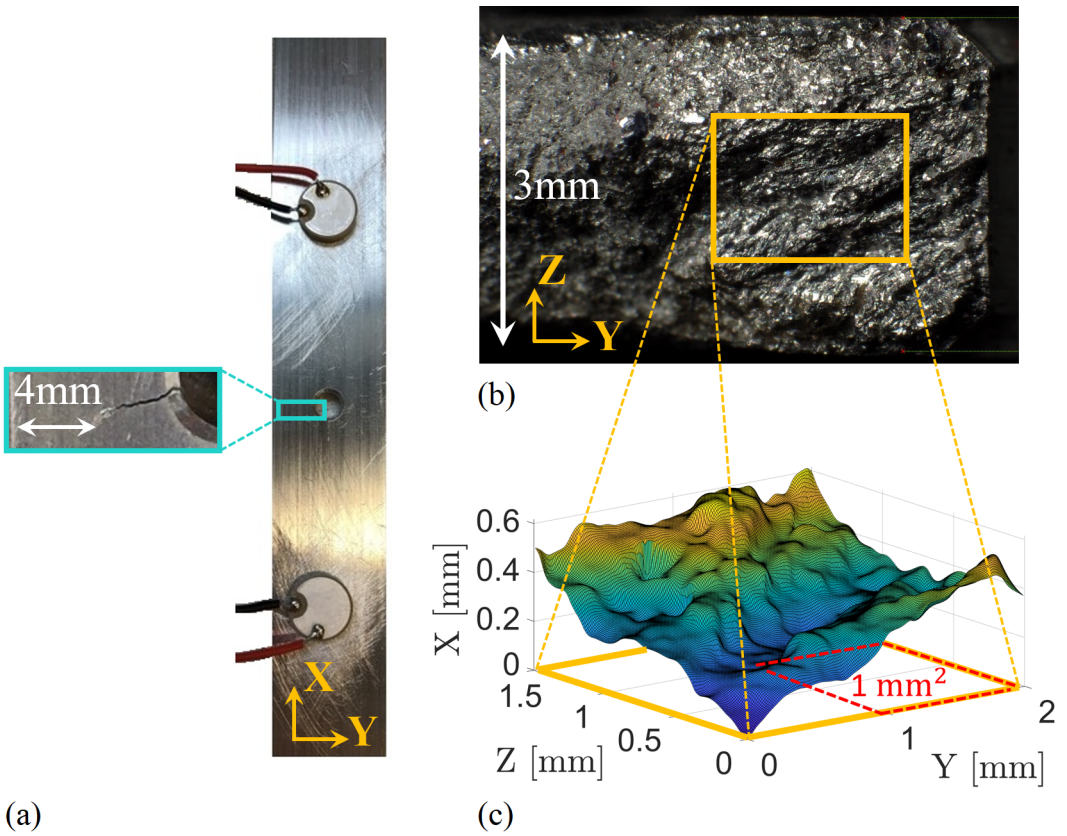

FIGURE 6.5: (a) Aluminum specimen with a fatigue crack initiating from the notch (b) Microscope image of the crack surface magnified with factor 1500 (c) Point cloud describing the measured three-dimensional geometry of the crack surface

Why should crack surfaces behave nonlinearly-elastic—and therefore cause modulation—in a purely tensile fatigue setup? Where does the contact between the crack surfaces come from under such conditions? The author aims to answer this question before demonstrating an approach to quantify the modulation caused by the local contact of fatigue crack surfaces.

To begin with, the rough surface of a local fatigue crack in aluminum[4] is looked upon closely with a microscope to measure its geometry. Figure 6.5a shows the aluminum specimen with a close-up of the fatigue crack that has initiated from the notch. After total fatigue failure of the specimen the crack surfaces are accessable for the microscope. A magnified image (factor 1500) is presented in figure 6.5b: The fatigue crack propagated from the right (notch) to the left in this image. A depth measurement (here in X-direction) is carried out with the microscope for a $2mm/1.5mm$ Y-Z-plane providing

[4]The material and geometry of this specimen are identical to the ones described previously. Fatigue loading was applied with $r = 0$ (tensile stress only). Total failure occurred after 52000 load cycles.

a point cloud, which describes the three-dimensional geometry of the crack surface. A three-dimensional plot of the data is given in figure 6.5c.

The point cloud data above the red dashed $1mm^2$ projection square in figure 6.5c is now utilized to define the nodes and elements of a FE mesh. The FE mesh describes a $1mm^3$ cube separated by the exact crack surface geometry that was measured experimentally. The FE mesh (node and element geometry) is exported to Abaqus CAE for further use (figure 6.6).

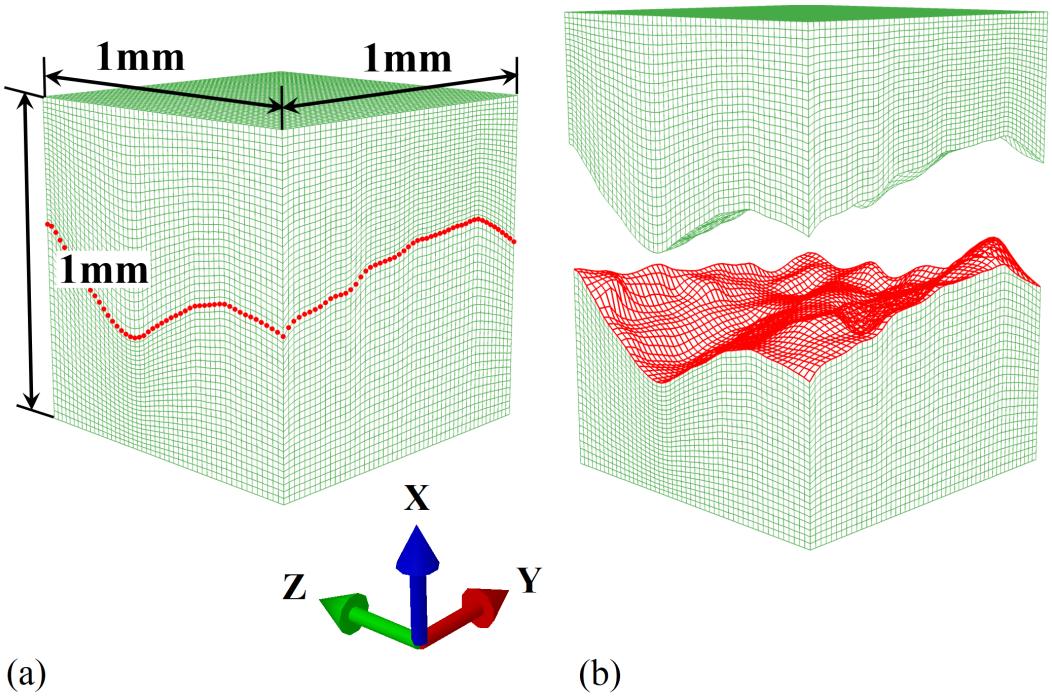

FIGURE 6.6: FE Model of a $1mm^3$ that is separated by the point cloud data (red) that represents the experimental crack surface geometry (a) Both cube parts in contact (perfect fit) (b) Both cube parts apart (in X-direction)

The crack surface of the lower cube part and the crack surface of the upper cube part are defined by the same point cloud data ensuring that they fit ideally into each other. Consequently, the parts can be in full contact (at each node) without any stress present.

The following considerations are made by the author to explain why such crack surfaces may exhibit nonlinear-elastic behavior even when the external fatigue loading is tensile only: Tensile stress must be present across the potential crack surfaces (here in X-direction) to cause cracking in the first place. After cracking, when the newly formed crack surfaces move apart for the first time, the geometry of the two surfaces are expected to be identical, as modelled in figure 6.6. These two crack surfaces will not be able to transfer any tensile stress and will behave linearly-elastic under pressure

in X-direction. Consequently, a bilinear-elastic behavior can be expected which—considering the explanation presented in chapter 3—does not lead to any modulation when fatigue loading is tensile only. However, in the author's opinion, the following question has to be raised: How likely is it that under tensile fatigue loading—repetitive opening and closing of the crack—these two surfaces find their way back into their original position perfectly? The author suggests the following two states that deviate from the ideal fit in reality:

1. A lateral respective shift of the crack surfaces (in Y-Z-plane)
2. Irreversible (and not identical) deformation of the crack surface geometry due to plastic deformation (lateral and/or longitudinal)

In the author's opinion it is very likely that both states above will happen to some extent when the tensile fatigue loading opens and closes the crack repetitively. This opinion is in line with most research articles on VAM indicating that the fatigue crack surfaces in metals are expected to be messy and chaotic [12].

In case the surfaces do not find their way back into the original position, the release of the external tensile force back to zero will activate local contact pressure at any location where the two surfaces deviate from a perfect fit. When the external force rises again, this local contact pressure will be reduced until the surfaces lose contact. It is this reduction of local contact pressure (under external tension) that can explain nonlinear-elastic behavior.

To demonstrate this, the upper cube part from figure 6.6 is shifted in Y- and Z-direction by 1/100 of the cube length ($\Delta Y = \Delta Z = 1mm/100 = 10\mu m$). The lateral offset is indicated in figure 6.7. It is too small to recognize it here. Now—with this lateral offset in place—a simulation is run where these two linear-elastic cube parts ($E = 7300kN/cm^2$) are pressed against each other vertically (in X-direction). To do so, all nodes at the bottom Y-Z-plane of the lower part are fixed in X-direction (boundary condition $u_X = 0$). The nodes at the top Y-Z-plane of the upper part behave as a rigid plate. This rigid plate is loaded by a prescribed vertical displacement moving downwards in negative X-direction (figure 6.7). During the simulation the reaction force in X-direction is measured. The results—vertical displacement of the rigid plate vs. the reaction force—are converted to stress vs. strain. The latter dependency is plotted in figure 6.8 (blue solid line). It can be observed that the system behaves indeed nonlinearly-elastic: In (nearly) full contact (strains

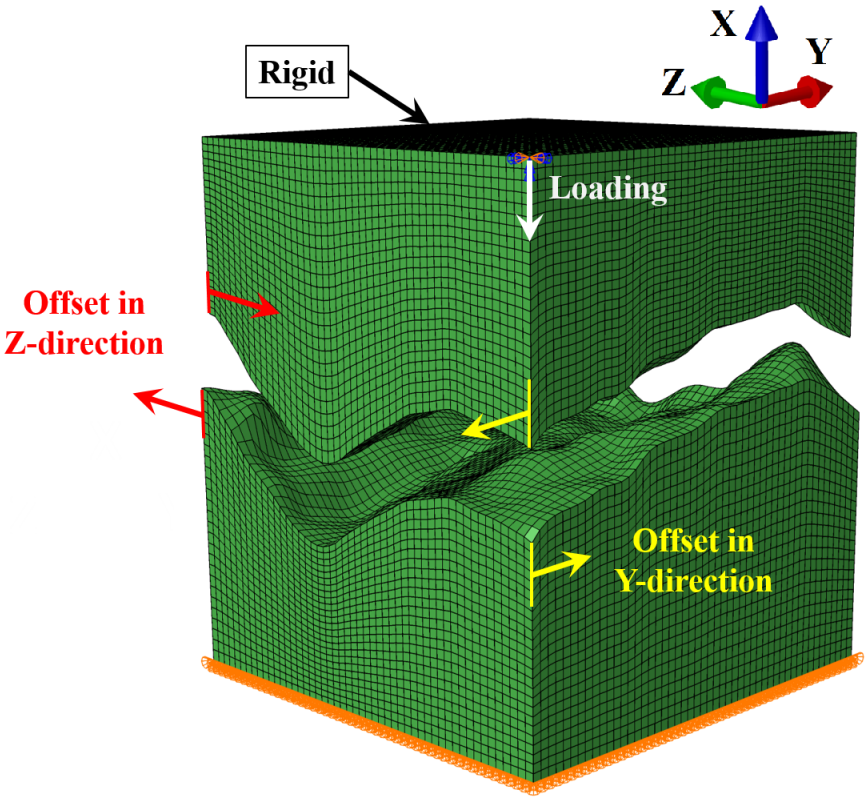

FIGURE 6.7: FE model of the separated cube with a lateral offset in Y- and Z-direction with $\Delta Y = \Delta Z = 1mm/100 = 10\mu m$; The top Y-Z-plane of the cube behaves as a rigid plate

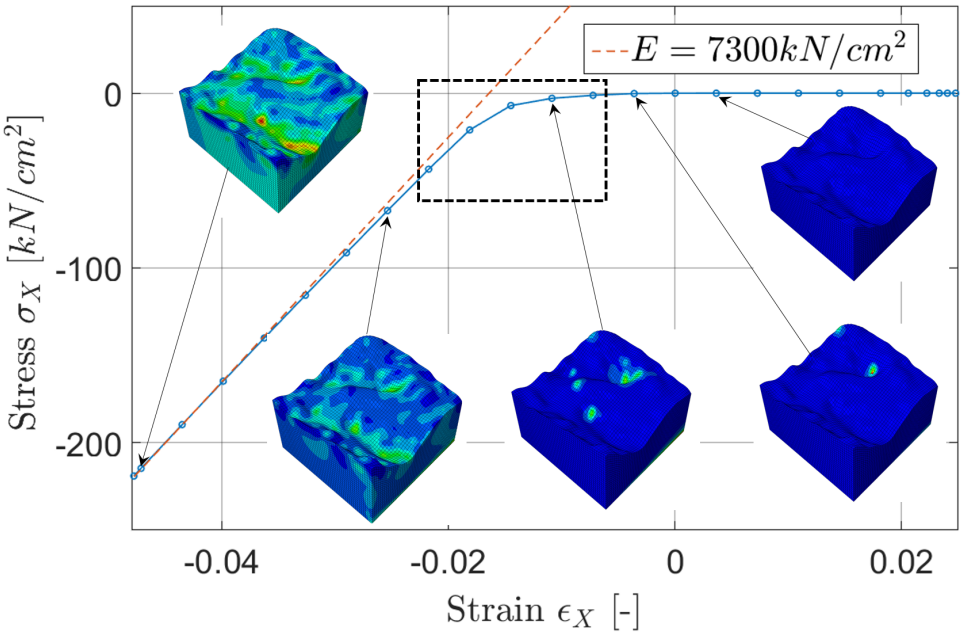

FIGURE 6.8: Stress vs. strain results (blue solid line) for the cube parts pressed against each other in X-direction (with the lateral offset); Linear reference (red dashed line) corresponding to the stiffness $E = 7300kN/cm^2$; The black dashed rectangle indicates the five data points that are used in the following step

$\epsilon < -0.04$) the stress-strain dependency approaches a linear function with a gradient corresponding to the Young's modulus that was set to the value $E = 7300kN/cm^2$ for the linear-elastic material. Once the crack surfaces lose contact entirely (strains $\epsilon > 0$) the stress-strain relationship becomes zero (constant). Between these two states ($-0.04 < \epsilon < 0$) the system behaves nonlinearly-elastic due to the variation of the contact surface transferring the load. Regarding this result, note three things: The position for $\epsilon = 0$ on the horizontal axis was chosen by the author to coincide with the initial contact of the two crack surfaces during post-processing. Second, the results in figure 6.8 show that the nonlinear behavior spans over a strain range of roughly $\Delta\epsilon = 0.04$. Within this strain range $\Delta\epsilon$ the gradient varies between the set Young's modulus E and zero ($E = 7300kN/cm^2 > gradient > 0kN/cm^2$). For this simulation the lateral offset was set to be $1/100$ of the cube length. Decreasing this offset will lead to results in which the strain span $\Delta\epsilon$ governing the nonlinear-elastic behavior will decrease, too. Such scaling of the nonlinear-elastic behavior is taken advantage of later in this section. Third, the results were developed for a $1mm^3$ cube. In the author's opinion the volume (and hereby the crack) can be extended in Y- and Z-direction without losing the validity of the stress-strain results in X-direction in figure 6.8.

At this point, it is understood why crack surfaces behave nonlinearly-elastic despite (external) tensile fatigue loading of the specimen. Further, the nonlinear-elastic behavior for an experimental crack geometry was demonstrated and quantified. In the following it is the goal to include the nonlinear-elastic behavior of the crack into the FE model of the aluminum specimen from sections 6.2 and 6.3 to investigate its effect on the system response (modulation).

To do so, two volumes (width $1mm$ in X-direction) are implemented in the FE model on both sides of the notch (s. figure 6.9a). Each of these volumes represent a volume that is separated by a fatigue crack. A total crack length of $6mm$ is considered here ($3mm$ on each side of the notch). The highlighted volumes are set to be nonlinear-elastic according to the prior results from the FE cube simulation with the following adjustments: Only five data points from figure 6.8 in the range $-0.022 < \epsilon < -0.007$ are used (enclosed by the black dashed rectangle in figure 6.8). This data is chosen, because it governs the strongly nonlinear-elastic behavior. The stresses σ_X and strains ϵ_X within it are scaled with factor 0.2 to ensure that the nonlinear behavior is fully activated during the simulation. The corresponding scaled stress-strain

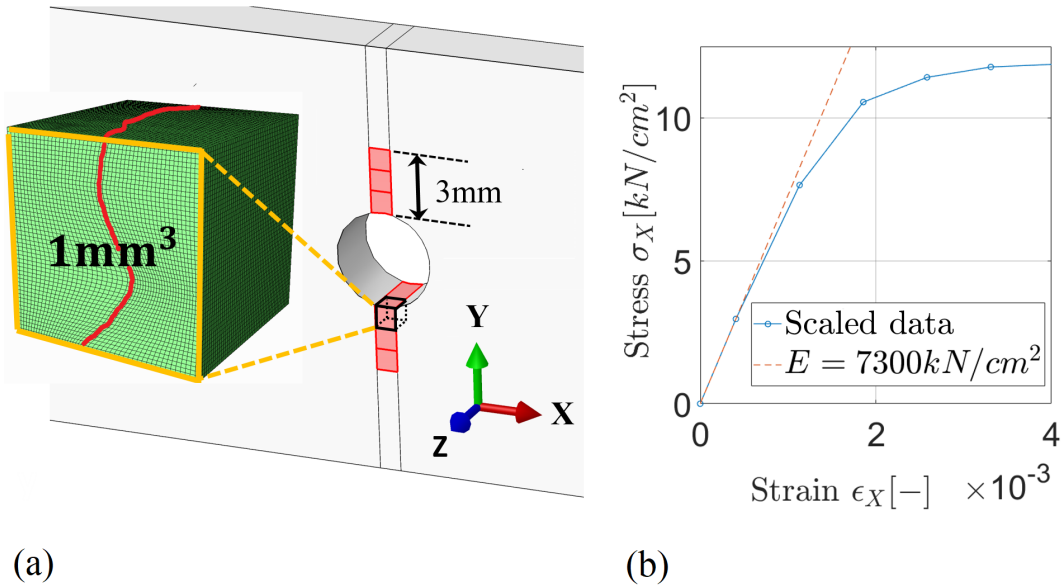

FIGURE 6.9: (a) Detail of the FE model around the notch: The highlighted red volumes represent volumes that are separated by a fatigue crack (b) Scaled stress-strain data (scaling factor 0.2) from the previous cube simulation. The data point in the origin (0,0) was added manually for reasons of comparison.

data (five points) are plotted in figure 6.9b. A sixth data point is added manually in the origin (0,0), so that the initial stiffness complies exactly with the Young's modulus $E = 7300kN/cm^2$ for reasons of comparison. By doing so, the author makes sure that when the LF excitation X_Ω approaches zero in the simulation, nonlinearity (3) the contact of fatigue crack surfaces does not affect the dynamic properties of the system.

In the next step, a simulation is run where the two red volumes in figure 6.9a behave according to the stress-strain data[5] in figure 6.9b while the rest of the specimen behaves linearly-elastic with $E = 7300kN/cm^2$. All other settings comply with the simulation from section 6.2. The results are plotted in figure 6.10.

The stress σ_X in closest vicinity of the sensing node is plotted in figure 6.10a and represents the LF excitation X_Ω. Figure 6.10b shows the coordinate system with the specimen in the FE model for orientation. In figure 6.10c the results from the first simulation only governing (1) the variation of geometric stiffness are presented with the corresponding FFT spectrum in dB in figure 6.10d. The results from the third simulation—governing (1) the variation of geometric stiffness and (3) the contact of fatigue crack surfaces—are shown

[5]Note that the red volumes in figure 6.9a are not actually separated by the fatigue crack in the FE model. Their nonlinear-elastic stress-strain dependency (figure 6.9b) takes into account the fatigue crack.

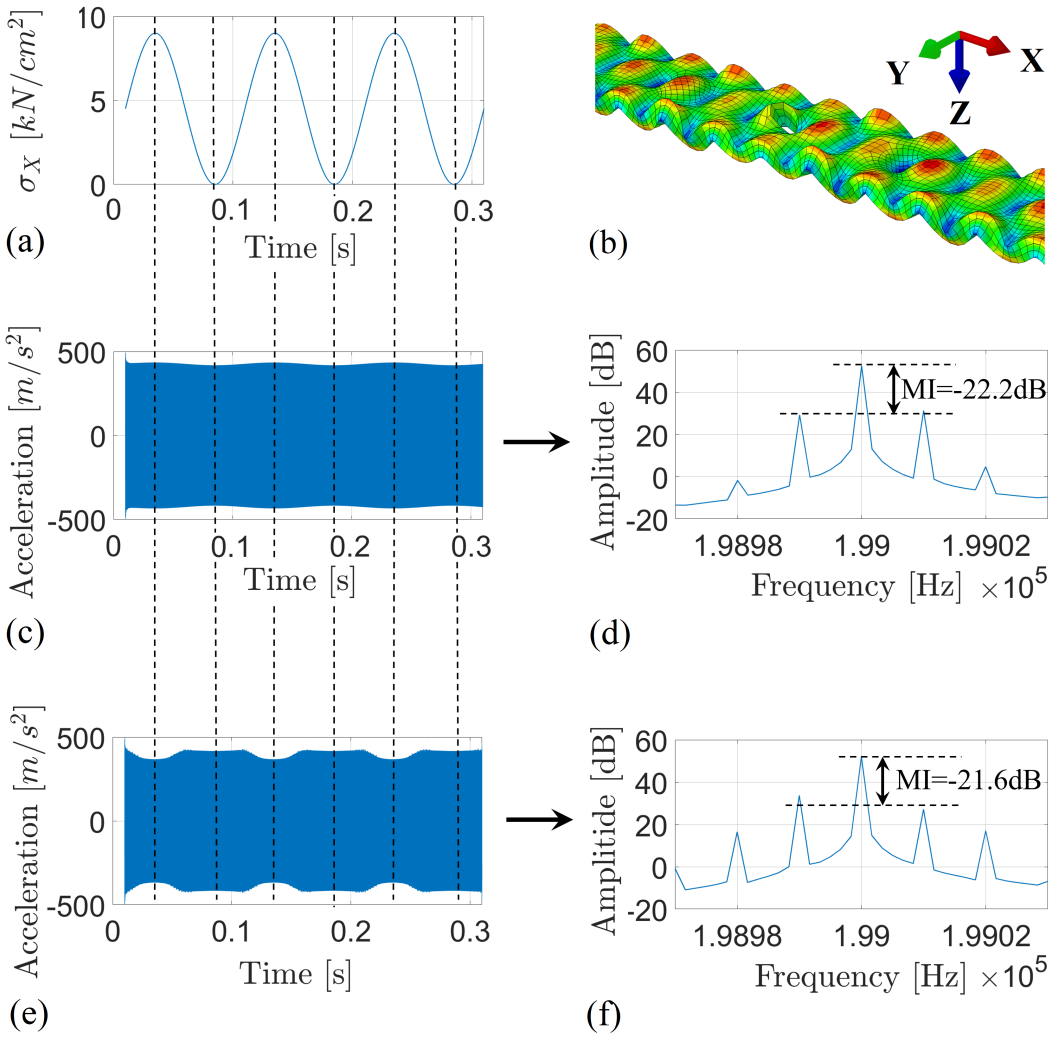

FIGURE 6.10: (a) Stress σ_X over time in direct vicinity of the sensing node (b) Coordinate system for orientation; deformation of the specimen is magnified by factor $2.5 \cdot 10^7$ (c) System response (acceleration in Z-direction) at the sensing node (the only present nonlinearity in this simulation is (1) the variation of geometric stiffness) (d) Corresponding FFT spectrum in *dB* (e) System response (acceleration in Z-direction) at the sensing node (the present nonlinearities in this simulation are (1) the variation of geometric stiffness and (3) the contact of fatigue crack surfaces) (f) Corresponding FFT spectrum in *dB*

analogously in figure 6.10e (system response in time domain) and figure 6.10f (FFT spectrum). When σ_X in figure 6.10a approaches zero, the nonlinearities do not affect the system properties. Therefore, the amplitudes in the corresponding system responses are identical for a moment.

It can be seen in time domain that the nonlinear behavior of such a small

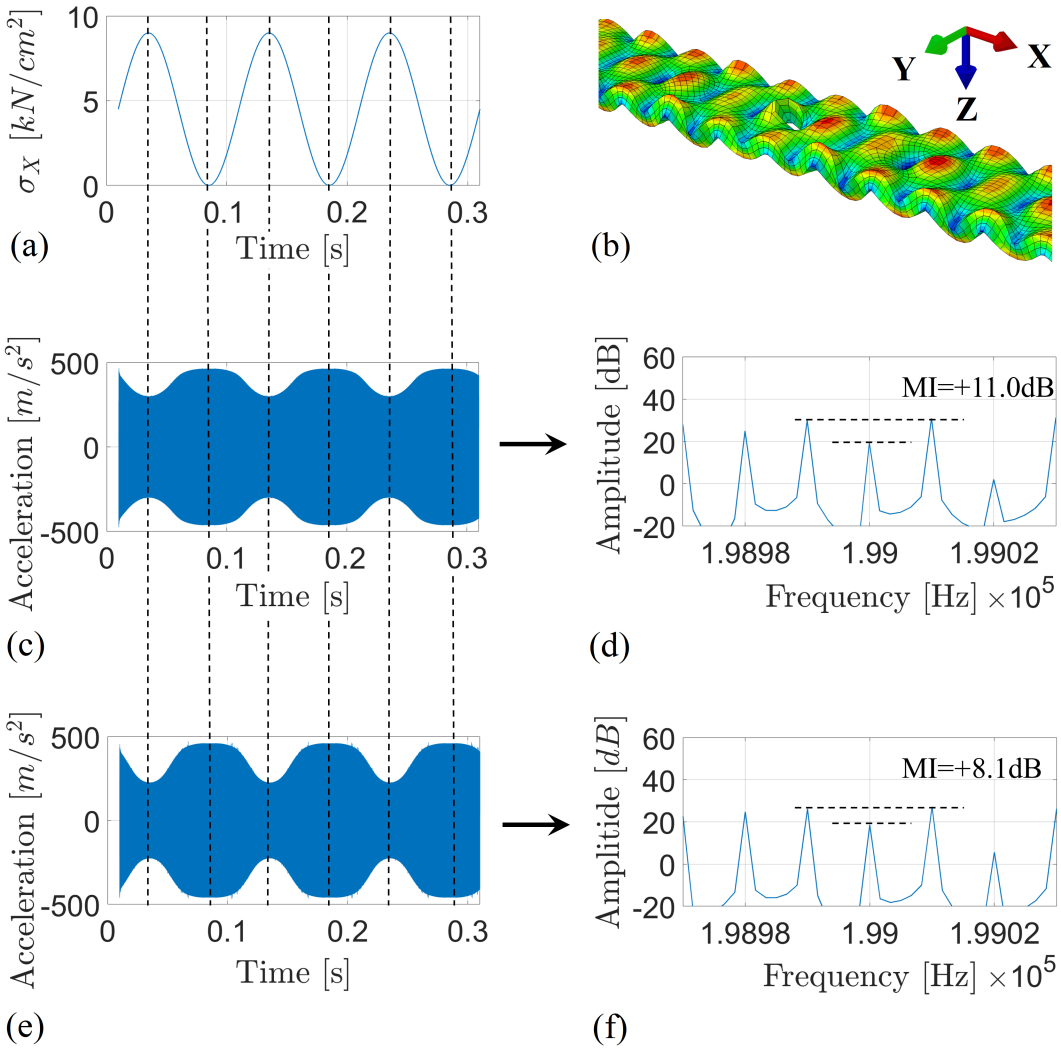

FIGURE 6.11: (a) Stress σ_X over time in direct vicinity of the sensing node (b) Coordinate system for orientation; deformation of the specimen is magnified by factor $2.5 \cdot 10^7$ (c) System response (acceleration in Z-direction) at the sensing node (the present nonlinearities in this simulation are (1) the variation of geometric stiffness and (2) the nonlinear-elastic behavior of aluminum) (d) Corresponding FFT spectrum in dB (e) System response (acceleration in Z-direction) at the sensing node (the present nonlinearities in this simulation are (1) the variation of geometric stiffness and (2) the nonlinear-elastic material behavior of aluminum and (3) the contact of fatigue crack surfaces) (f) Corresponding FFT spectrum in dB

volume affects the global system response significantly in terms of modulation. Note that also in this case the AM caused by (1) the variation of geometric stiffness and (3) the contact of fatigue crack surfaces work in opposite directions, as expected on the basis of the suggested physical explanation. In fact, this result demonstrates that the modulation caused by (3) the contact of fatigue crack surfaces is significantly stronger than the modulation caused

by (1) the variation of geometric stiffness. If the nonlinearities were equally strong, the modulations would neutralize each other. Conventional quantification of the spectrum with $MI = -21.6dB$ would not allow detection of the fatigue crack, because the increase $\Delta MI = 0.6dB$ is negligibly small. This demonstrates that the conventional evaluation technique is error prone.

Finally, a simulation is run with all three nonlinearities combined in the same system. The results are plotted in figure 6.11e and 6.11f. Figure 6.11c and 6.11d show the results from the simulation only governing the first two nonlinearities (the variation of geometric stiffness and the nonlinear-elastic behavior of aluminum). Comparison of the results in time domain (figure 6.11c vs. 6.11e) reveals that the "additional" nonlinearity introduced by the fatigue crack increases the AM in the system response. The MIs evaluated from the corresponding FFT spectra, however, do not display such an increase in terms of modulation. In fact, evaluation of the spectrum in 6.11d (without crack) leads to the value $MI = +11.0dB$ while the spectrum in figure 6.11f (with crack) only leads to the value $MI = +8.1dB$. Note that the spectra from both simulations show over one hundred pairs of sidebands governing the modulation. The MI however only takes into account the first pair at $\omega \pm \Omega$. This demonstrates that an additional nonlinearity in the system (here: the crack) does not necessarily increase the MI. It emphasizes the prior conclusion that the conventional monitoring approach is error prone.

6.5 Discussion

Three nonlinearities were investigated separately. The first nonlinearity—the variation of geometric stiffness—is displayed in the FE simulation naturally. In case of the second nonlinearity—the nonlinear-elastic material behavior of aluminum—experimental test data was taken into account to model it accurately. For the third nonlinearity—the contact of fatigue crack surfaces—experimental microscope data was presented that describes the three-dimensional geometry of a fatigue crack surface in aluminum. The geometry was used to explain and demonstrate numerically why and how nonlinear such contact may behave under (external) tensile fatigue loading. The results were utilized to define the nonlinear-elastic material of a local volume in the model representing the crack.

Numerical simulations were carried out to quantify the modulation contributed by the three individual nonlinearities to the system response for the

aluminum specimen under tensile fatigue loading. Comparison of the results showed that the nonlinear-elastic behavior of aluminum and the contact of fatigue crack surfaces (total crack length $6mm$) cause both significantly stronger modulation than the variation of geometric stiffness in this system. Interestingly, it was observed that both cause AM which works contrarily to the AM due to the variation of geometric stiffness. This demonstrates the validity of the fourth analytical finding that was presented in section 5.4: Different nonlinearities can work in opposite directions. The physical explanation from chapter 3 can explain this phenomenon comprehensively: The geometric stiffness increases when the external tensile force is rising. Both other nonlinearities behave the opposite way: The nonlinear-elastic behavior of aluminum and the contact of fatigue crack surfaces behave softer with increasing tensile load. Therefore, the natural frequency is affected in opposite ways. Consequently, the amplitude and the phase are affected contrarily by these nonlinearities.

Most VAM studies measure a baseline modulation at a time when the structure is expected to be pristine. This baseline modulation is used as a reference value. Later, during the lifetime of the structure, the modulation is measured and compared to the reference. The initiation and growth of structural damage is expected to increase the modulation in the system response. Taking into account the new finding this procedure appears error prone: Consider a system with perfectly linear-elastic material where the baseline modulation of the pristine specimen is primarily caused by the harmonic variation of geometric stiffness. The initiation and growth of a fatigue crack would decrease (and neutralize) this modulation before it can increase it. The sidebands' amplitudes and the MI would drop until the modulation of both nonlinearities are equally strong.

The final simulation with all three nonlinearities combined in the same system revealed that the "additional" nonlinearity introduced by the crack does increase the AM in time domain. However, the MI—only taking into account the first pair of sidebands—does not necessarily display such an increase. This result emphasizes the prior conclusion that the conventional monitoring approach has to be reconsidered. The presented investigations and findings in this chapter can be the basis to develop new evaluation techniques for SHM applications with VAM offering superior reliability and robustness.

Chapter 7

Summary and outlook

A physical explanation was suggested explaining why any elastic nonlinearity may cause vibro-acoustic modulation (VAM) in a dynamic system that is excited by two waves (X_ω and X_Ω) simultaneously with frequencies that differ significantly ($\omega >> \Omega$): The LF vibration X_Ω activates the nonlinearity and varies quasi-statically the natural frequency ω_0 corresponding to the dominant mode shape. The amplitude and phase of the ultrasonic system response depend on the natural frequency ω_0 and are therefore modulated with low frequency Ω. This analytical explanation is built upon the assumption that the system reaches a steady-state vibration (constant amplitude and phase over time) due to ultrasonic excitation X_ω before the LF vibration X_Ω can change the dynamic properties of the system significantly. The fulfillment of the assumption was validated experimentally and numerically for an aluminum plate-like structure and excitation frequencies $\Omega = 10Hz \cdot 2\pi$ and $180kHz \cdot 2\pi < \omega < 230kHz \cdot 2\pi$.

Five analytical findings were concluded from the physical explanation: 1) Any elastic nonlinearity may cause amplitude modulation (AM) and phase modulation (PM) at the same time, because both result from a variation of the natural frequency $\omega_0(\Omega)$. 2) The temporal coincidence of the envelope function with the loading state $F(\Omega)$ depends on the ultrasonic excitation frequency ω. The maximum amplitude of the envelope function can either coincide with the minimum or the maximum loading F, depending on wether the ratio $\beta = \omega/\omega_0$ is varied above or below the value $\beta = 1.0$. This phenomenon was demonstrated experimentally and numerically for the investigated aluminum structure. 3) There is a variety of envelope functions that can appear in VAM applications that differ qualitatively from a "sine-like" shape. The occurrence of such envelope functions was demonstrated experimentally and numerically. The suggested physical explanation was employed to explain all of them comprehensively. 4) Two different nonlinearities combined in the same system can cause contrary AM and PM. This

finding was demonstrated numerically. It was concluded that the conventional VAM evaluation quantifying sideband amplitudes to detect and monitor structural damage is error prone. 5) The fulfillment of the major assumption stated previously enables the artificial computation of the modulated system response from at least two steady-state vibration measurements. This approach might enable VAM applications without the excitation of the LF vibration X_Ω potentially reducing the necessary data by 98%.

Three nonlinearities in the system mentioned previously were investigated separately: The variation of geometric stiffness, the nonlinear-elastic behavior of aluminum and the contact of fatigue crack surfaces. The modulation caused by them individually was quantified and compared by carrying out numerical simulations. It was shown that all three nonlinearities cause significant modulation in the investigated system. The modulations caused by the nonlinear-elastic behavior of aluminum and the contact of fatigue crack surfaces were observed to be contrary to the modulation caused by the variation of geometric stiffness. This result demonstrated the fourth analytical finding derived from the physical explanation. It emphasizes the conclusion that the conventional VAM evaluation is error prone and might explain its insufficient reliability.

The findings in this dissertation indicate that new evaluation techniques focusing on the time domain might offer improved reliability and sensitivity. On the basis of the presented work, the author suggests to carry out parameter studies in a subsequent step: How do different geometries, materials, sensor positions and excitation frequencies influence the amount of modulation in the system response (in time domain)? These investigations should be carried out for each nonlinearity in the system separately. Further, the author would examine how the modulation contributions by the single nonlinearities in the system correlate with the LF amplitude A_Ω. If they do not correlate similarly, one could optimize the amplitude A_Ω for a specific structure, so that damage-induced modulation is strong while non-damage-induced modulations are as weak as possible to boost reliability and sensitivity. The fifth analytical finding regarding artificial computation of the modulated system response from at least two steady-state vibration measurements should be exploited and discussed in future works.

The author hopes that this dissertation helps the scientific community to take another step towards developing powerful and robust methods that utilize the nonlinear behavior of structural damage to improve safety and sustainability.

Appendix A

Analytical computations of AM and PM

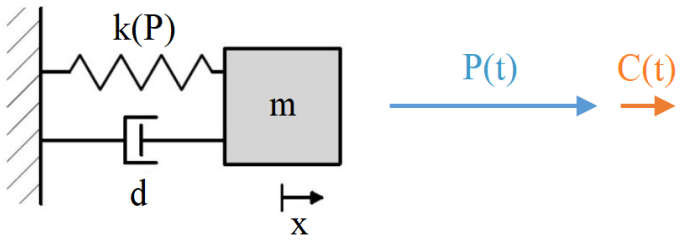

FIGURE A.1: SDOF system with mass m, damping coefficient d and stiffness $k(P)$. The system is excited simultaneously by a low frequency wave $P(t)$ and an ultrasonic wave $C(t)$.

Figure A.1 shows a SDOF system, described by the mass m, the damping coefficient d and the stiffness k. The system is excited by two waves simultaneously. One of them is the LF vibration $P(t)$ with angular frequency Ω and amplitude A_Ω (equation A.1). The other one is the ultrasonic wave $C(t)$ with angular frequency ω and amplitude A_ω (equation A.2). It is assumed that $\omega >> \Omega$ and $A_\omega << A_\Omega$.

$$P(t) = A_\Omega \cdot cos(\Omega t) \tag{A.1}$$

$$C(t) = A_\omega \cdot cos(\omega t) \tag{A.2}$$

The nonlinearity of the SDOF system lies in the circumstance that the stiffness k depends on the force P. The dependency of k on P is assumed to be linear here (equation A.3) where k_0 is the initial stiffness value (constant) and $-a$ is the gradient of the linear dependency. This dependency is chosen as a simple example. Note that the analytical computations in the following work for any given relationship $k(P)$. The effect of C on the stiffness k is negligible, because $A_\omega << A_\Omega$.

$$k(P) = k_0 - a \cdot P \tag{A.3}$$

By substituting (A.1) into (A.3) one obtains the time-dependent stiffness $k(t)$, as shown in equation A.4.

$$k(t) = k_0 - a \cdot A_\Omega \cdot cos(\Omega t) \tag{A.4}$$

The natural frequency ω_0 of the SDOF is given in equation A.5 and the damping ratio ξ in equation A.6 [11].

$$\omega_0 = \sqrt{\frac{k}{m}} \tag{A.5}$$

$$\xi = \frac{d}{2m\omega_0} \tag{A.6}$$

By substituting A.4 into A.5, the natural frequency ω_0 becomes time-dependent (A.7):

$$\omega_0(t) = \sqrt{\frac{k_0 - a \cdot A_\Omega \cdot cos(\Omega t)}{m}} \tag{A.7}$$

By substituting A.7 into A.6, also the damping ratio ξ becomes time-dependent (A.8).

$$\xi(t) = \frac{d}{2m\sqrt{\frac{k_0 - a \cdot A_\Omega \cdot cos(\Omega t)}{m}}} \tag{A.8}$$

The analytical solutions for the amplitude D and the phase θ of the steady-state response regarding excitation with the ultrasonic wave $C(t)$ with frequency ω are known [11]. The amplitude D is given in equation A.9, the phase θ in equation A.10.

$$D = \frac{1}{\sqrt{\left(1 - \left(\frac{\omega}{\omega_0}\right)^2\right)^2 + \left(2\xi\frac{\omega}{\omega_0}\right)^2}} \tag{A.9}$$

$$\theta = arctan\frac{2\xi\frac{\omega}{\omega_0}}{1 - \left(\frac{\omega}{\omega_0}\right)^2} \tag{A.10}$$

By substituting A.7 and A.8 into A.9 and into A.12, the amplitude D and the phase θ become functions of time (A.11 and A.12). $D(t)$ is the envelope

function of the system response, representing AM. The function $\theta(t)$ represents PM.

$$D(t) = \frac{1}{\sqrt{\left(1 - \frac{\omega^2}{\frac{k_0 - a \cdot A_\Omega \cdot cos(\Omega t)}{m}}\right)^2 + \left(\frac{d\omega}{k_0 - a \cdot A_\Omega \cdot cos(\Omega t)}\right)^2}} \tag{A.11}$$

$$\theta(t) = arctan \frac{\frac{d\omega}{k_0 - a \cdot A_\Omega \cdot cos(\Omega t)}}{1 - \frac{m\omega^2}{k_0 - a \cdot A_\Omega \cdot cos(\Omega t)}} \tag{A.12}$$

The resulting system response $S(t)$ exhibiting AM and PM is given in equation A.13.

$$S(t) = D(t) \cdot cos(\omega t + \theta(t)) \tag{A.13}$$

Bibliography

[1] A. Alnutayfat, A. M. Sutin, and D. Liu. "Vibroacoustic Modulation of Wideband Vibrations and Its Possible Application for Windmill Blade Diagnostics". In: *International Journal of Civil and Environmental Engineering* 2023.17 (2023), pp. 31–36.

[2] A. Alnutayfat et al. "Sideband Peak Count in a Vibro-Acoustic Modulation Method for Crack Detection". In: *Acoustics* 4.1 (2022), pp. 74–86. DOI: 10.3390/acoustics4010005.

[3] F. Aymerich and W. J. Staszewski. "Experimental Study of Impact-Damage Detection in Composite Laminates using a Cross-Modulation Vibro-Acoustic Technique". In: *Structural Health Monitoring: An International Journal* 9.6 (2010), pp. 541–553. ISSN: 1475-9217. DOI: 10.1177/1475921710365433.

[4] A. Baltazar. "On the relationship between ultrasonic and micromechanical properties of contacting rough surfaces". In: *Journal of the Mechanics and Physics of Solids* 50.7 (2002), pp. 1397–1416. ISSN: 00225096. DOI: 10.1016/S0022-5096(01)00119-3.

[5] B. Boll et al. "Synthetic generation of vibroacoustic modulation signals for structural health monitoring applications". In: *Mech. Syst. Signal Process.* under Review (2023).

[6] B. Boll et al. "Weak adhesion detection – Enhancing the analysis of vibroacoustic modulation by machine learning". In: *Composite Structures* 273 (2021), p. 114233. ISSN: 02638223. DOI: 10.1016/j.compstruct.2021.114233.

[7] C. Boller, F.-K. Chang, and Y. Fujino, eds. *Encyclopedia of Structural Health Monitoring*. Chichester, UK: John Wiley & Sons, Ltd, 2009. ISBN: 9780470-058220. DOI: 10.1002/9780470061626.

[8] D. Broda et al. "Modelling of nonlinear crack–wave interactions for damage detection based on ultrasound—A review". In: *Journal of Sound and Vibration* 333.4 (2014), pp. 1097–1118. ISSN: 0022460X. DOI: 10.1016/j.jsv.2013.09.033.

[9] D. Broda et al. “The Study of Localized Crack-Induced Effects of Nonlinear Vibro-Acoustic Modulation”. In: *Materials (Basel, Switzerland)* 16.4 (2023), p. 1653. ISSN: 1996-1944. DOI: 10.3390/ma16041653.

[10] X. J. Chen et al. “Characterization of progressive microcracking in Portland cement mortar using nonlinear ultrasonics”. In: *NDT & E International* 41.2 (2008), pp. 112–118. ISSN: 09638695. DOI: 10.1016/j.ndteint.2007.08.009.

[11] R. W. Clough and J. Penzien. *Dynamics of structures*. 2. ed., reprint. New York: McGraw-Hill, 2004. ISBN: 9780071132411.

[12] D. M. Donskoy. “Nonlinear Acoustic Methods”. In: *Encyclopedia of Structural Health Monitoring*. Ed. by C. Boller, F.-K. Chang, and Y. Fujino. Vol. 1. Chichester, UK: John Wiley & Sons, Ltd, 2009. ISBN: 9780470058220.

[13] D. M. Donskoy and D. Liu. “Vibro-acoustic modulation baseline-free non-destructive testing”. In: *Journal of Sound and Vibration* (2020), p. 115808. ISSN: 0022460X. DOI: 10.1016/j.jsv.2020.115808.

[14] D. M. Donskoy and M. Ramezani. “Separation of amplitude and frequency modulations in Vibro-Acoustic Modulation Nondestructive Testing Method”. In: Proceedings of Meetings on Acoustics. Acoustical Society of America, 2018, p. 045002.

[15] D. M. Donskoy and A. M. Sutin. “Vibro-Acoustic Modulation Nondestructive Evaluation Technique”. In: *Journal of Intelligent Material Systems and Structures* 9.9 (1998), pp. 765–771. ISSN: 1045-389X. DOI: 10.1177/1045389X9800900909.

[16] D. M. Donskoy, A. M. Sutin, and A. E. Ekimov. “Nonlinear acoustic interaction on contact interfaces and its use for nondestructive testing”. In: *NDT & E International* 34.4 (2001), pp. 231–238. ISSN: 09638695. DOI: 10.1016/S0963-8695(00)00063-3.

[17] D. M. Donskoy et al. “A Nonlinear Acoustic Technique for Crack and Corrosion Detection in Reinforced Concrete”. In: *Nondestructive Characterization of Materials VIII*. Ed. by Robert E. Green. Boston, MA: Springer US, 1998, pp. 555–560. ISBN: 978-1-4613-7198-4. DOI: 10.1007/978-1-4615-4847-8{\textunderscore}87.

[18] D. M. Donskoy et al. “Vibro-acoustic amplitude and frequency modulations during fatigue damage evolution”. In: AIP Conference Proceedings. Author(s), 2019, p. 040004. DOI: 10.1063/1.5099754.

[19] L. Dorendorf, N. Lalkovski, and M. Rutner. "Physical explanation for vibro-acoustic modulation due to local and global nonlinearities in a structure and its experimental and numerical validation". In: *Journal of Sound and Vibration* 528 (2022), p. 116885. ISSN: 0022460X. DOI: 10.1016/j.jsv.2022.116885.

[20] P. Duffour, M. Morbidini, and P. Cawley. "A study of the vibro-acoustic modulation technique for the detection of cracks in metals". In: *The Journal of the Acoustical Society of America* 119.3 (2006), p. 1463. ISSN: 0001-4966. DOI: 10.1121/1.2161429. URL: https://asa.scitation.org/doi/pdf/10.1121/1.2161429.

[21] M. Dunn et al. "Critical Aspects of Experimental Damage Detection Methodologies Using Nonlinear Vibro-ultrasonics". In: *Procedia Engineering* 188 (2017), pp. 133–140. ISSN: 18777058. DOI: 10.1016/j.proeng.2017.04.466.

[22] K. Dziedziech et al. "Efficient swept sine chirp excitation in the nonlinear vibro-acoustic wave modulation technique used for damage detection". In: *Structural Health Monitoring: An International Journal* 17.3 (2018), pp. 565–576. ISSN: 1475-9217. DOI: 10.1177/1475921717704638.

[23] K. Dziedziech et al. "Experimental study of thermo-acoustic wave modulation in a cracked plate". In: *Journal of Sound and Vibration* 498 (2021), p. 115970. ISSN: 0022460X. DOI: 10.1016/j.jsv.2021.115970.

[24] A. E. Ekimov, I. N. Didenkulov, and V. v. Kazakov. "Modulation of torsional waves in a rod with a crack". In: *The Journal of the Acoustical Society of America* 106.3 (1999), pp. 1289–1292. ISSN: 0001-4966. DOI: 10.1121/1.427163.

[25] J. Górski et al. "Identification of the stick and slip motion between contact surfaces using artificial neural networks". In: *Nonlinear Dynamics* 100.1 (2020), pp. 225–242. ISSN: 0924-090X. DOI: 10.1007/s11071-020-05515-8.

[26] Y. He et al. "Contact acoustic nonlinearity effect on the vibro-acoustic modulation of delaminated composite structures". In: *Mechanical Systems and Signal Processing* 163 (2022), p. 108161. ISSN: 08883270. DOI: 10.1016/j.ymssp.2021.108161.

[27] H. F. Hu et al. "Crack detection using nonlinear acoustics and piezoceramic transducers—instantaneous amplitude and frequency analysis".

In: *Smart Materials and Structures* 19.6 (2010), p. 065017. ISSN: 0964-1726. DOI: 10.1088/0964-1726/19/6/065017.

[28] Z.D. Jastrzebski. *The Nature and Properties of Engineering Materials*. Wiley, 1987. ISBN: 9780471818410.

[29] K.-Y. Jhang. "Erratum to: Nonlinear ultrasonic techniques for nondestructive assessment of micro damage in material: A review". In: *International Journal of Precision Engineering and Manufacturing* 18.1 (2009), p. 139. ISSN: 2234-7593. DOI: 10.1007/s12541-017-0018-3.

[30] P. Karve and S. Mahadevan. "On the performance of vibro–acoustic–modulation–based diagnosis of breathing cracks in thick, elastic slabs". In: *Structural Control and Health Monitoring* 27.3 (2020). ISSN: 1545-2255. DOI: 10.1002/stc.2470.

[31] P. Karve et al. "Vibro-acoustic modulation and data fusion for localizing alkali–silica reaction–induced damage in concrete". In: *Structural Health Monitoring: An International Journal* 19.6 (2020), pp. 1905–1923. ISSN: 1475-9217. DOI: 10.1177/1475921720905509.

[32] J.-Y. Kim, V. A. Yakovlev, and S. I. Rokhlin. "Parametric modulation mechanism of surface acoustic wave on a partially closed crack". In: *Applied Physics Letters* 82.19 (2003), p. 3203. ISSN: 0003-6951. DOI: 10.1063/1.1572552. URL: https://aip.scitation.org/doi/pdf/10.1063/1.1572552.

[33] S. Kim et al. "Crack detection technique for operating wind turbine blades using Vibro-Acoustic Modulation". In: *Structural Health Monitoring: An International Journal* 13.6 (2014), pp. 660–670. ISSN: 1475-9217. DOI: 10.1177/1475921714553732.

[34] Y. Kim, H. J. Lim, and H. Sohn. "Nonlinear ultrasonic modulation based failure warning for aluminum plates subject to fatigue loading". In: *International Journal of Fatigue* 114 (2018), pp. 130–137. ISSN: 01421123. DOI: 10.1016/j.ijfatigue.2018.05.014.

[35] A. Klepka, J. Mrówka, and J. Górski. "Experimental investigation of modulation effects for contact-type interfaces in vibro-acoustic modulation tests". In: *Structural Health Monitoring: An International Journal* 20.3 (2021), pp. 917–930. ISSN: 1475-9217. DOI: 10.1177/1475921719857624.

[36] A. Klepka et al. "Impact damage detection in laminated composites by non-linear vibro-acoustic wave modulations". In: *Composites Part B: Engineering* 65 (2014), pp. 99–108. ISSN: 13598368. DOI: 10.1016/j.compositesb.2013.11.003.

[37] A. Klepka et al. "Nonlinear acoustics for fatigue crack detection – experimental investigations of vibro-acoustic wave modulations". In: *Structural Health Monitoring: An International Journal* 11.2 (2012), pp. 197–211. ISSN: 1475-9217. DOI: 10.1177/1475921711414236.

[38] J. Li et al. "Artificial Intelligence (AI)-Based Evaluation of Bolt Loosening Using Vibro-Acoustic Modulation (VAM) Features from a Combination of Simulation and Experiments". In: *Applied Sciences* 12.24 (2022), p. 12920. DOI: 10.3390/app122412920.

[39] H. J. Lim and H. Sohn. "Necessary Conditions for Nonlinear Ultrasonic Modulation Generation Given a Localized Fatigue Crack in a Plate-Like Structure". In: *Materials (Basel, Switzerland)* 10.3 (2017). ISSN: 1996-1944. DOI: 10.3390/ma10030248.

[40] H. J. Lim, H. Sohn, and Y. Kim. "Data-driven fatigue crack quantification and prognosis using nonlinear ultrasonic modulation". In: *Mechanical Systems and Signal Processing* 109 (2018), pp. 185–195. ISSN: 08883270. DOI: 10.1016/j.ymssp.2018.03.003.

[41] B. Liu, J. Yang, and T. Gang. "Analysis of sound and vibration interaction on a crack and its use in high-frequency parameter selection for vibro-acoustic modulation testing". In: *Mechanical Systems and Signal Processing* 143 (2020), p. 106835. ISSN: 08883270. DOI: 10.1016/j.ymssp.2020.106835.

[42] D. Liu and D. M. Donskoy. "Frequency-modulation-in-vibro-acoustic-modulation-method". In: *International Journal of Civil and Environmental Engineering* Vol:17, No:1 (2023).

[43] P. Liu et al. "Baseline-free fatigue crack detection based on spectral correlation and nonlinear wave modulation". In: *Smart Materials and Structures* 25.12 (2016), p. 125034. ISSN: 0964-1726. DOI: 10.1088/0964-1726/25/12/125034.

[44] M. Meo, U. Polimeno, and G. Zumpano. "Detecting Damage in Composite Material Using Nonlinear Elastic Wave Spectroscopy Methods". In: *Applied Composite Materials* 15.3 (2008), pp. 115–126. ISSN: 0929-189X. DOI: 10.1007/s10443-008-9061-7.

[45] S. Miele et al. “Diagnosis of internal cracks in concrete using vibro-acoustic modulation and machine learning”. In: *Structural Health Monitoring: An International Journal* 21.5 (2022), pp. 1973–1991. ISSN: 1475-9217. DOI: 10.1177/14759217211047901.

[46] P. B. Nagy. “Fatigue damage assessment by nonlinear ultrasonic materials characterization”. In: *Ultrasonics* 36.1-5 (1998), pp. 375–381. DOI: 10.1016/S0041-624X(97)00040-1.

[47] V. E. Nazarov and A. M. Sutin. “Nonlinear elastic constants of solids with cracks”. In: *The Journal of the Acoustical Society of America* 102.6 (1997), pp. 3349–3354. ISSN: 0001-4966. DOI: 10.1121/1.419577.

[48] T. Ooijevaar et al. “Vibro-acoustic modulation–based damage identification in a composite skin–stiffener structure”. In: *Structural Health Monitoring: An International Journal* 15.4 (2016), pp. 458–472. ISSN: 1475-9217. DOI: 10.1177/1475921716645107.

[49] P. Oppermann et al. “Nonlinear modulation with low-power sensor networks using undersampling”. In: *Structural Health Monitoring: An International Journal* (2021), p. 147592172098288. ISSN: 1475-9217. DOI: 10.1177/1475921720982885.

[50] Z. Parsons and W. J. Staszewski. “Nonlinear acoustics with low-profile piezoceramic excitation for crack detection in metallic structures”. In: *Smart Materials and Structures* 15.4 (2006), pp. 1110–1118. ISSN: 0964-1726. DOI: 10.1088/0964-1726/15/4/025.

[51] *PI Ceramics - Piezo Product PRYY+0372 Data Sheet*. https://static.piceramic.com/fileadmin/user_upload/physik_instrumente/files/datasheets/disc-Datasheet.pdf. Accessed: 2022-01-28.

[52] L. Pieczonka et al. “Damage imaging in composites using nonlinear vibro-acoustic wave modulations”. In: *Structural Control and Health Monitoring* 25.2 (2018), e2063. ISSN: 1545-2255. DOI: 10.1002/stc.2063.

[53] L. Pieczonka et al. “Nonlinear vibroacoustic wave modulations for structural damage detection: an overview”. In: *Optical Engineering* 55.1 (2016), p. 011005. ISSN: 0091-3286. DOI: 10.1117/1.OE.55.1.011005.

[54] U. Polimeno and M. Meo. “Understanding the effect of boundary conditions on damage identification process when using non-linear elastic wave spectroscopy methods”. In: *International Journal of Non-Linear Mechanics* 43.3 (2008), pp. 187–193. ISSN: 00207462. DOI: 10.1016/j.ijnonlinmec.2007.12.013.

[55] O. Rudenko and A. Chin. "Nonlinear acoustic properties of a rough surface contact and acoustiodiagnostics of a roughness height distribution". In: *Acoustical Physics* 1994 (1994).

[56] SIMULIA. *Abaqus 6.14 Documentation - Abaqus Analysis User's Guide*. Dassault Systemes. Vélizy-Villacoublay, France, 2014.

[57] A. K. Singh et al. "A theoretical and numerical study on the mechanics of vibro-acoustic modulation". In: *The Journal of the Acoustical Society of America* 141.4 (2017), p. 2821. ISSN: 0001-4966. DOI: 10.1121/1.4981133.

[58] I. Y. Solodov, N. Krohn, and G. Busse. "CAN: an example of nonclassical acoustic nonlinearity in solids". In: *Ultrasonics* 40.1-8 (2002), pp. 621–625. DOI: 10.1016/S0041-624X(02)00186-5.

[59] German Institute for Standardization. *DIN 50125:2016-12, Testing of metallic materials – Tensile test pieces*.

[60] L. Straka et al. "Detection of structural damage of aluminum alloy 6082 using elastic wave modulation spectroscopy". In: *NDT & E International* 41.7 (2008), pp. 554–563. ISSN: 09638695. DOI: 10.1016/j.ndteint.2008.04.004.

[61] K. E.-A. van den Abeele, P. A. Johnson, and A. Sutin. "Nonlinear Elastic Wave Spectroscopy (NEWS) Techniques to Discern Material Damage, Part I: Nonlinear Wave Modulation Spectroscopy (NWMS)". In: *Research in Nondestructive Evaluation* 12.1 (2000), pp. 17–30. ISSN: 0934-9847. DOI: 10.1080/09349840009409646.

[62] K. E.-A. van den Abeele et al. "Micro-damage diagnostics using nonlinear elastic wave spectroscopy (NEWS)". In: *NDT & E International* 34.4 (2001), pp. 239–248. ISSN: 09638695. DOI: 10.1016/S0963-8695(00)00064-5.

[63] L. Wei and J. Chen. "Determination of optimal probing frequency for enhancing nonlinear vibro-acoustic modulation behaviors of delaminated CFRP based on local defect resonance". In: *Mechanical Systems and Signal Processing* 187 (2023), p. 109961. ISSN: 08883270. DOI: 10.1016/j.ymssp.2022.109961.

[64] T. Yin, C.-T. Ng, and A. Kotousov. "Damage detection of ultra-high-performance fibre-reinforced concrete using a harmonic wave modulation technique". In: *Construction and Building Materials* 313 (2021), p. 125306. ISSN: 09500618. DOI: 10.1016/j.conbuildmat.2021.125306.

[65] T. Yin et al. “Amplitude-Modulation Vibro-Acoustic Technique for Damage Evaluation”. In: *Structural Health Monitoring: An International Journal* (2022), p. 147592172211062. ISSN: 1475-9217. DOI: 10.1177/14759217221106209.

[66] N. C. Yoder and D. E. Adams. “Vibro-Acoustic Modulation Utilizing a Swept Probing Signal for Robust Crack Detection”. In: *Structural Health Monitoring: An International Journal* 9.3 (2010), pp. 257–267. ISSN: 1475-9217. DOI: 10.1177/1475921710365261.

[67] V. Y. Zaitsev, V. Gusev, and B. Castagnède. “Observation of the "Luxemburg-Gorky effect" for elastic waves”. In: *Ultrasonics* 40.1-8 (2002), pp. 627–631. DOI: 10.1016/S0041-624X(02)00187-7.

[68] V. Y. Zaitsev, L. A. Matveev, and A. L. Matveyev. “On the ultimate sensitivity of nonlinear-modulation method of crack detection”. In: *NDT & E International* 42.7 (2009), pp. 622–629. ISSN: 09638695. DOI: 10.1016/j.ndteint.2009.05.001.

[69] V. Y. Zaitsev and P. Sas. “Nonlinear Response of a Weakly Damaged Metal Sample: A Dissipative Modulation Mechanism of Vibro-Acoustic Interaction”. In: *Journal of Vibration and Control* 6.6 (2000), pp. 803–822. ISSN: 1077-5463. DOI: 10.1177/107754630000600601.

[70] V. Y. Zaitsev et al. “Nonlinear Interaction of Acoustical Waves Due to Cracks and Its Possible Usage for Cracks Detection”. In: *Modal Analysis* 1.3 (1995), pp. 335–344. ISSN: 1066-0763. DOI: 10.1177/107754639500100305.

[71] V. Y. Zaitsev et al. “Novel nonlinear-modulation acoustic technique for crack detection”. In: *NDT & E International* 39.3 (2006), pp. 184–194. ISSN: 09638695. DOI: 10.1016/j.ndteint.2005.07.007.